Contents

5. Atmospheric Structure

C.H. Humphrey
Visidyne, Inc.
Burlington, Mass.

C.R. Philbrick
Air Force Geophysics Laboratory
Hanscom Air Force Base, Mass.

S.M. Silverman
Air Force Geophysics Laboratory
Hanscom Air Force Base, Mass.

T.F. Tuan
University of Cincinnati
Cincinnati, Ohio

M. Anapol
S.S.G., Inc.
Waltham, Mass.

J.B. Kumer
Lockheed Missles and Space Corp.
Palo Alto, Calif.

1. INTRODUCTION

In addition to the long-term variations of the atmospheric species concentrations and temperature described in Chapter 3, the atmosphere is subject to variations that have shorter periods and smaller spatial wavelengths. These variations in species concentrations and temperature can result in fluctuations of the resultant infrared intensity that can effect the interpretation of infrared measurements. In this chapter we review information concerning these variations and draw some conclusions as to the magnitude and size of the spatial structures as functions of altitude.

A preliminary model for the calculation of the noise (that is, the clutter) created in infrared measuring systems due to the effects of random spatial structures on the radiant intensity is also discussed. In addition, we shall briefly discuss auroral emissions and a model showing how spatial fluctuations in TV all-sky photometric measurements of visible aurora radiation can be used to generate spatial power spectral densities of the auroral infrared radiance.

2. SOURCES OF ATMOSPHERIC STRUCTURE

Dynamic effects such as tides and gravity waves can perturb a "quiet static" atmosphere. The sources of these dynamic effects can be associated with a very large variety of phenomenon, such as absorption of solar radiation by atmospheric species, solar heating of the surface, sunspot variations, magnetospheric substorms, particle events, severe tropospheric disturbances, planetary waves, wind-induced waves from interaction with orographic features, earthquakes, and volcanic eruptions or artificially produced phenomenon such as bomb explosions.

2.1 Tidal Effects

Large-scale tidal oscillations of the atmosphere are produced mainly by the thermal action resulting from the absorption of solar radiation in the stratosphere and lower mesosphere. That the very strong semidiurnal component in the barometric variation was due mainly to the sun's heating was first recognized by Laplace. The present inviscid tidal theory is based on the classical work of Siebert (1954)[1] and Sen and White, (1955),[2] who were the first to consider atmospheric heating rather than heating by upward eddy conduction from the ground. Siebert found that absorption by H_2O can account for 1/3 of the large semidiurnal component while absorption by O_3 can account for the remaining two thirds. The large semidiurnal component of pressure at the ground level, relative to the diurnal component, and the higher values of the diurnal component in the middle and upper atmosphere are explained on the basis that heating from O_3 absorption does not reach ground.

---

1. Siebert, M. (1954) Zur theoric der thermischen erregung gezeitenaitiger schwingunger der erdatmosphare. Z. Naturwissenschaften 41:446.
2. Sen, H.K. and White, M.L. (1955) Thermal and gravitational excitation of atmospheric oscillations, J. Geophys. Res. 60:483-485.

For a basic treatment of tidal wave theory the reader is referred to Chapman and Lindzen (1970).[3] Recent theoretical advances in tidal wave theory deal mainly with the addition of such effects as mean zonal winds, meridional temperature gradients, composition variations, and hydromagnetic coupling, as well as dissipative effects such as molecular viscosity, thermal conductivity, radiative damping, and ion drag. For a review that considers some of these recent advances see Forbes and Garrett (1978).[4] The empirical classification of the observed tides, as well as the theoretical treatment, is generally done in the form of harmonic analysis. However, owing to weather and seasonal changes, the dependent variables, such as pressure or temperature, are not quite cyclic on a day-to-day basis. In the thermosphere where ion drag, viscosity, and heat conduction are important, there is no such thing as a pure tidal mode.

The tidal effects on an otherwise unperturbed atmosphere produce inhomogeneities in optical emission and composition of various atmospheric species, some of which can take part in reactions involving infrared radiation bands. The effects on the emission of the green line of atomic oxygen (557.7 nm) were considered by Forbes and Geller (1972)[5] and Petitdidier and Teitelbaum (1977).[6] Assuming the Chapman three-body recombination mechanism for molecular oxygen and chemical equilibrium, the green line intensity is proportional to the cube of the atomic oxygen density. Forbes and Geller (1972)[5] determined the variation of (O) with lunar tide from the continuity equation neglecting production and loss. They concluded that the lunar tide is sufficient to produce a variation in the green line airglow similar to that observed. Petitdidier and Teitelbaum (1977)[6] considered the effects of solar thermal tides. They assumed that the composition of the atmosphere remains unchanged under the influence of the tidal wave and used a model that assumes a sinusoidal variation of the relative density in terms of time and space. Using a vertical wavelength of 45 km and a period of 12 h, that is, a semidiurnal tide, Petitdidier and Teitelbaum obtained intensity ratios (I_{min}/I_{max}) in fair agreement with observed data.[6] They were also able to fit observed OH experimental data with a semidiurnal tide. This analysis did not give a very sensitive test to the tidal wave theory since they compared only the total column intensity ratios. The formation of OH from the reaction

---

[3] Chapman, S., and Lindzen, R.S. (1970) Atmospheric Tides, D. Reidel, Hingham, Mass.

[4] Forbes, J.M. and Garrett, H.B. (1978) Solar diurnal tide in the thermosphere, J. Atmos. Sci. 35:148-208.

[5] Forbes, J.M. and Geller, M.A. (1972) Lunar semidiurnal variation in OI (5577A) nightglow, J. Geophys. Res. 77:2942-2947.

[6] Petitdidier, M. and Teitelbaum, H. (1977) Lower thermosphere emissions and tides, Planet Space Sci. 25:711-721.

$$H + O_3 \rightarrow OH + O_2 \qquad (1)$$

is dependent on the concentrations of the minor species H and O_3 that are influenced by the tidal wave. The assumption that the atmospheric composition is not influenced by the tidal wave is only true for major species.

Diurnal variations in the concentrations of H, He, O, O_2, N_2, and Ar due to energy sources in the lower atmosphere and, in particular the EUV, have been considered by Harris and Mayr (1975,[7] 1977[8]). Their calculations are based on a two-component model in which the two components are the major species N_2 and O. This treatment assumes, that while the major components may impart momentum to the minor components, the minor components do not physically or chemically affect the major components in any way. Their results show that the most important contribution to the diurnal variation is the thermal expansion followed by wind-induced diffusion that, in fact, dominates the diurnal variation of He and prevails strongly in the variations of O, O_2, and Ar below 200 km.

Forbes (1978)[9] and Forbes and Garrett (1978)[4] used a single component N_2 as the major species and all other constituents, that include O, O_2, Ar, He, and H, as minor species. The minor species were coupled to the major species through collision. Special emphasis is placed in their calculations on the diurnal and semidiurnal variations at sunspot maximum and minimum. Their results show that, between the equator and the midlatitude, the diurnal tidal variation in the thermospheric composition depends, at a given height, more strongly on the solar cycle than on the latitudinal position. The opposite is true for the semidiurnal tidal variations, where they find a major dependence with latitude in the semidiurnal amplitude and phase. These effects are presently not modeled in the J77 and MSIS models. Differences in the total density variations between equatorial and middle latitudes are predicted by this theory (Forbes and Marcos, 1979)[10] to be of the order of 20 - 50 percent in amplitude and 3 - 6 h in phase for the semidiurnal component, 0-20 percent in amplitude and 0-6 h in phase for the diurnal component, and 15 km in the altitude of transition from semidiurnal to diurnal

---

[7] Harris, I. and Mayr, H.G. (1975) Diurnal variations in the thermosphere, J. Geophys. Res. 80:3925-3933.

[8] Mayr, H.G. and Harris, I. (1977) Diurnal tide, composition, and winds, J. Geophys. Res. 82:2628-2640

[9] Forbes, J.M. (1978) Tidal variations in thermospheric O, O_2, N_2, Ar, He and H, J. Geophys. Res. 83:3691-3698.

[10] Forbes, J.M. and Marcos, F.A. (1979) Seasonal-latitudinal tidal structures of O, N_2, and total mass density in the thermosphere, J. Geophys. Res. 84:31-35.

predominance. Experimental data that supports their results is presented in the next section.

2.2 Atmospheric Gravity Waves

Gravity waves are atmospheric waves with frequencies lower than the natural oscillation of the atmosphere, the Brunt-Vaisala frequency, that has a period ranging from less than 5 min to 15 min. For a gravity wave the pressure gradient, which may be along any direction, is modified by the influence of gravitational and buoyant forces that are along the vertical direction. Since the frequency of the wave is less than the Brunt-Vaisala frequency, the influence of the gravity and buoyancy forces begin to manifest themselves and the wave is no longer in the direction of the pressure gradient. For a free gravity wave in an isothermal atmosphere an upward transfer of energy (group velocity) is always accompanied by a downward phase propagation and vice versa (Hines, 1960).[11]

As far as introducing variabilities and inhomogeneties, there are three main features that distinguish gravity waves from the tides. These features are: 1) gravity waves can often have length scales of the order of 6 to 8 km (for example, vertical wavelength) that are considerably less than the length scales of tidal waves, 2) gravity waves can have time scales of the order of 10 min to two or three hours that are considerably less than the time scales of dirunal or semidiurnal tides, and 3) gravity waves occur randomly, unlike the tides that occur regularly due to solar heating of the atmosphere.

The effects of gravity waves were initially detected in microbaragraphs at the ground level, airglow measurements from various altitudes in the atmosphere, and ionospheric radar measurements from higher altitudes. Recent techniques allow high resolution in-situ measurements of the effects of gravity waves. The earliest observations were made indirectly through their effects on the ionosphere called traveling ionosphere disturbances (TID). Georges (1968)[12] characterized the spectrum of observed TID into two distinct categories of waves: 1) the large-scale TID's have horizontal phase velocities greater than 350-400 m/sec and horizontal wavelengths exceeding 1000 km and 2) the medium-scale TID's have horizontal phase velocities commonly between 100 and 250 m/sec and horizontal wavelengths of the order of several hundred km's. They occur much more frequently than the large-scale TID's. The significant contribution in establishing that these large-scale TID's are caused by gravity waves was made by Thome (1968),[13] who

---

11. Hines, C.O. (1960) Internal atmospheric gravity waves at ionospheric heights, Can. J. Phys. 38:1441-1481.

12. Georges, T.M. (1968) HF Doppler studies of traveling ionospheric disturbances, J.Atmos. Terr. Phys. 30:735.

13. Thome, G.D. (1968) Long-period waves generated in the polar ionosphere during the onset of magnetic storms, J. Geophys. Res. 73:6319-6336.

used the measurements of incoherent radar backscatter from different altitudes in the ionosphere as a function of time.

Gravity waves have also been detected from their effects on airglow emission. Many of the airglow emissions (for example, O 557.7 nm line, OH, etc.) have their peak intensities well below the peak of the ionospheric F-layer. This allows studies to be made over larger altitude ranges whenever the airglow data can be combined with the ionospheric data [for example, Dachs (1968)[14] and Armstrong (1975)[15]]. Airglow data showing wave-like structures have been published by numerous people including Silverman (1962),[16] Okuda (1962),[17] and Dachs (1968).[14] Dach's data (1968)[14] include observations on the O lines at 557.7 nm and 630.0 nm as well as simultaneous observations of various ionospheric parameters such as the altitude of the F2 peak h'F2 and the lowest penetration frequency at the peak $f^{o}F2$.

The basic paper on gravity-wave theory is due to Hines (1960),[11] who assumed an inviscid uniform isothermal atmosphere. Even with such drastic assumptions this treatment provides a reasonably good first approximation for gravity waves with low horizontal phase velocities (less than 150 m/sec). For higher horizontal phase velocities the treatment breaks down as atmospheric structure begins to have an effect. Investigations of the acoustic gravity equations for a more realistic atmosphere show the presence of fully guided modes [Press and Harkrider (1962),[18] Pfeffer and Zarichny (1963),[19] Harkrider and Wells (1968)[20]] as well as partially guided or leakage modes [Friedman (1966),[21] Reddy (1969)[22]]. The

---

14. Dachs, J. (1968) Die helligkeiten des nachtlichen luftleuchtens wahrend des sommerflechen minimums nach messungen in Sudwestafrika, Beitr. Phys. d. Atmosphare 41:184-215.
15. Armstrong, E.B. (1975) The influence of a gravity wave on the airglow hydroxyl rotational temperature at night, J. Atmos. Terr. Phys. 37:1585-1592.
16. Silverman, S.M. (1962) Unusual fluctuations of 5577 Å O I airglow emission intensity on October 28-29, 1961, Nature 195:481-482.
17. Okuda, M. (1962) A study of excitation process in night airglow, Sci. Rep. Tohoku Univ. 5th Ser. Geophysics, 14:9-26.
18. Press, F. and Harkrider, D.G. (1962) Propagation of acoustic-gravity waves in the atmosphere, J. Geophys. Res. 67:3889-3908.
19. Pfeffer, R.L., and Zarichny, J. (1963) Acoustic-gravity wave propagation in an atmosphere with two sound channels, Pure and Appl Geophys. 55:175-199.
20. Harkrider, D.G. and Wells, F.J. (1968) Acoustic-Gravity Waves in the Atmosphere-Symposium Proceedings, T.M. Georges, (ed.) U.S. Government Printing Office, Washington, D.C., pp. 299-314.
21. Friedman, J.P. (1966) Propagation of internal gravity waves in a thermally stratified atmosphere, J. Geophys. Res. 71:1033-1054.
22. Reddy, C.A. (1969) Internal Gravity and Acoustic Waves, A Colloquium, NCAR-TN-43, pp. 229-240.

inclusion of dissipation can produce additional partially guided modes [Tuan (1976),[23] Richmond (1978)[24]]. In general, inhomogeneities can scatter gravity waves and hence, may (although not necessarily) produce additional guided modes.

Both for the case of the tidal waves and gravity waves the theories have been mainly tested against the observed temporal variations in the optical emission. The effect of gravity waves on the atmospheric emission of the O 630 nm and the N 520 nm lines was treated theoretically by Porter, Silverman, and Tuan (1974)[25] with satisfactory agreement between theory and experimental data. Spatial inhomogeneities have been observed in OH emission by Peterson and Kieffaber [Peterson and Kieffaber (1973),[26] Kieffaber and Peterson (1978)[27]]. They found well defined OH structures to occur near the time of high lunar tide. Peterson (1979)[28] suggested that these structures may have been caused by gravity wave interactions in the OH layer. Gravity wave effects on any optical emission depend on the atmospheric minor constituents redistribution caused by the wave. The major constituents are assumed to move with the wave while the effects of the wave on the minor components are through collisions with the major constituents.

Chiu and Ching (1978)[29] have considered the general features that a Hines (1960)[11] gravity wave model will have on a minor atmospheric component whose density distribution is in the form of a single layer. Their summary of the conclusions of various authors are 1) the response of the layer to the gravity wave is sharper at the bottom side than at the top side, 2) there is a 180° phase change in the response of the minor constituent in going from the bottom to the top side, and 3) the magnitude of the response depends on the gradient of the unperturbed layer. The sharper the gradient, the sharper becomes the response.

---

23. Tuan, T. F. (1976) Research in Gravity Waves and Airglow Phenomena, AFGL-TR-76-0296, AD A040 414.

Richmond, A. D. (1978) Gravity wave generation, propagation and dissipation in the thermosphere, J. Geophys. Res. 83:4131-4145.

25. Porter, H. S., Silverman, S. M. and Tuan, T. F. (1974) On the behavior of airglow under the influence of gravity waves, J. Geophys. Res. 79: 3827-3833.

26. Peterson, A. W. and Kieffaber, L. M. (1973) Infrared photography of OH airglow structures, Nature 242:321-323.

27. Kieffaber, L. H. and Peterson, A. W. (1978) Correlation studies of four submicron OH airglow bands during spacelab simulation, J. Atmos. Terr. Phys. 40:1339-1345.

28. Peterson, A. W. (1979) Airglow events visible to the naked eye, Applied Optics 18:3390-3393.

29. Chiu, Y. T. and Ching, B. K. (1978) The response of atmospheric and lower ionospheric layer structures to gravity waves, Geophys. Res. Lett. 5:539-542.

Recently, Hatfield et al (1981)[30] studied the variability of the OH emission produced by gravity waves. Their results indicate that structure in the emission profile could occur if the vertical wavelength of the gravity wave is less than the "width" of the emission profile. This corresponds to gravity waves with horizontal phase velocities less than 33 m/sec. Guided modes usually have much greater horizontal phase velocities and hence, much larger vertical wavelength and can only affect the integrated columnar emission as a function of time. Thus, gravity waves can always produce temporal inhomogeneities, but only those with small horizontal phase velocities and vertical wavelength of less than 10 km can produce spatial as well as temporal inhomogeneities.

Further studies on the fluctuation of OH and $O_2(^1\Sigma)$ airglow have been made by Weinstock (1978).[31] He found that for $O_2(^1\Sigma)$ the temperature dependence of the reaction rate constant has a major influence on the temporal inhomogeneities.

Spatial and temporal inhomogeneities can be generated by atmospheric gravity waves if the energy of the waves is dissipated in forming a layer of turbulence [Hodges (1967)[32]]. In some cases it is possible to show that large amplitude gravity waves with a Richardson's number less than one-half can parametrically excite Brunt-Vaisala oscillations (Tuan, et al, 1979[33]). This means that temporal inhomogeneities of the relatively short time scales of Brunt-Vaisala oscillations (of the order of 4-12 min) are superimposed on inhomogeneities of the larger time scales (or the order of hours) of the gravity wave oscillations.

Gravity waves that are usually present in the middle and upper atmosphere are frequently associated with sources in the lower atmosphere. At times this wave propagation can be effectively cut off from the upper atmosphere by reflection or dissipation processes in the mesosphere. However, sources in the upper atmosphere also exists. An indication of the horizontal and vertical wavelengths of gravity waves in the mesosphere and the lower thermosphere is given in Figure 1 (Philbrick et al, 1978[34]). Also shown are the viscous dissipation limits for

---

30. Hatfield, R., Tuan, T.F. and Silverman, S.M. (1981) On the effects of atmospheric gravity waves on profiles of H, O_3, and OH emission, J. Geophys. Res. 80:2429-2437.

31. Wienstock, J. (1978) Theory of the interaction of gravity waves with $O_2(^1\Sigma)$ airglow, J. Geophys. Res. 83:5175-5185.

32. Hodges, R.R. (1967) Generation of turbulence in the upper atmosphere by internal gravity waves, J. Geophys. Res. 72:3455-3458.

33. Tuan, T.F., Hedinger, R., Silverman, S.M. and Okuda, M. (1979) On gravity wave induced Brunt-Vaisala oscillations, J. Geophys. Res. 84:393-398.

34. Philbrick, C.R., Noonan, J.P., Fletcher, [illegible], Jr., Hanrahan, T., Salah, J.E., Blood, D.W., Olsen, R.O. [illegible] Kennedy, B.W. (1978) Atmospheric Properties From Measurements at Kwajalein Atoll on 5 April 1978, AFGL-TR-0195, AD A061 083.

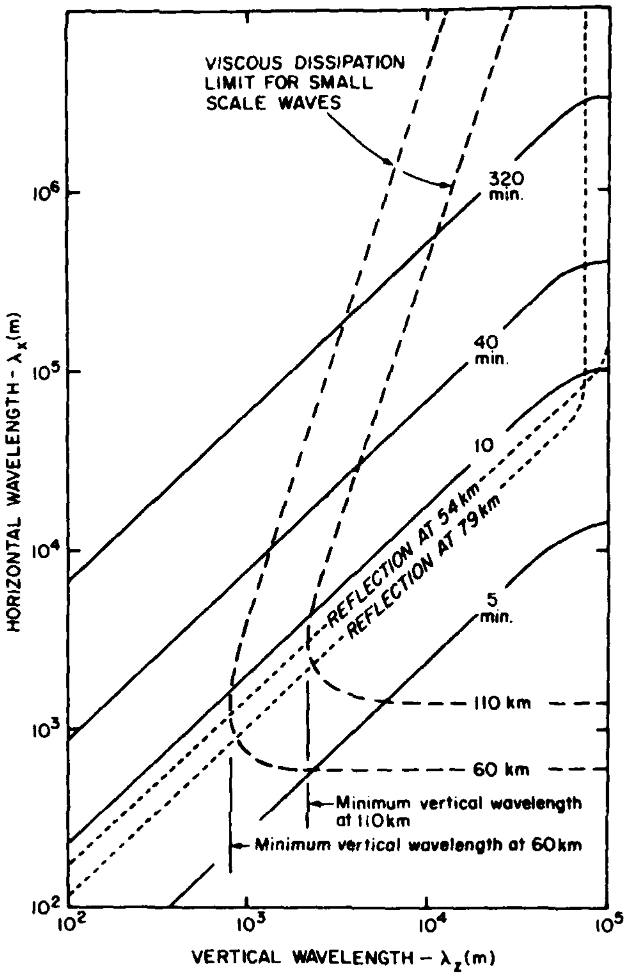

Figure 1. Wavelengths of Propagating Modes Expected in the Mesosphere and Lower Thermosphere From a Reexamination of the Analysis of Hines[35] With Inclusion of Eddy Viscosity Contribution. The periods in min are shown as constant period contours (solid lines). The viscous dissipation limit for small-scale waves at 60 and 110 km are shown (dash lines) and represent the limits of the permitted spectrum from effects of viscous damping (modes lying to the left and below these curves are excluded). Modes subject to reflection back toward the ground at heights of 54 and 79 km are indicated (dot lines) and modes lying to the right of these curves cannot proceed from the lower atmosphere (Philbrick et al, 1978[34]).

---

[35] Hines, C.O. (1974) The Upper Atmosphere in Motion, American Geophysical Union Monograph 18.

small-scale waves and the limits for modes subject to reflection back toward the ground. From Figure 1 we see that gravity waves propagating in the region from 60 to 110 km altitude will have wavelengths larger than 1 km at 60 km and larger than 3 km at 110 km.

Gravity waves may be produced by a number of mechanisms including orographic features such as mountain ranges, tropospheric disturbances such as thunderstorms, and localized pressure gradients produced by auroral heating in the mesosphere and lower thermosphere. Studies have been made by Davis and Da Rosa (1969)[36] on the frequency of occurrence of gravity waves produced by magnetic storms. The observations for the year 1967 showed a close correlation between the occurrence of TID's and severe magnetic storms ($K_p > 5$). For smaller storms there was far less correlation. These results are in good agreement with those of Georges (1968)[12] and Thome (1968)[13] who suggested a relationship between enhanced magnetic activity and the occurrence of large-scale TID's.

In general, there has been little investigation on the frequency of occurrence of gravity waves due to other sources. If the theory as advanced by Hodges (1967)[32] that gravity waves are an important factor in producing upper atmospheric turbulence is correct, then the frequency of occurrence must be much greater than that from magnetic storms.

3. ATMOSPHERE STRUCTURE MEASUREMENTS

3.1 Tidal Effects

The effects produced by the thermally driven tides in the upper atmosphere present another important consideration. Recently Forbes and Marcos (1979)[10] analyzed total mass density data from the miniature electrostatic accelerometer (Mesa) experiment on the AE-E satellite to determine diurnal and semidiurnal tidal variations in the lower thermosphere (150-245 km) at latitudes less than 20°. The results of the analysis showed that structure changes from predominantly semidiurnal below 180 ±5 km to predominantly diurnal above this altitude, with no strong dependence on season. These results are in agreement with recent theoretical (Mayr and Harris, 1977,[8] Forbes, 1978[9]) and observational (Newton et al, 1975[37] Sharp et al, 1978[38]) investigations (see Figure 2). The analysis by Forbes and Marcos showed a substantial summer/winter difference in the phase structure of the semidiurnal component of the total mass density variation.[10] The results indicate that the combination of data from all seasons to determine an

---

References 36 to 38 will not be listed here. See References, page 114.

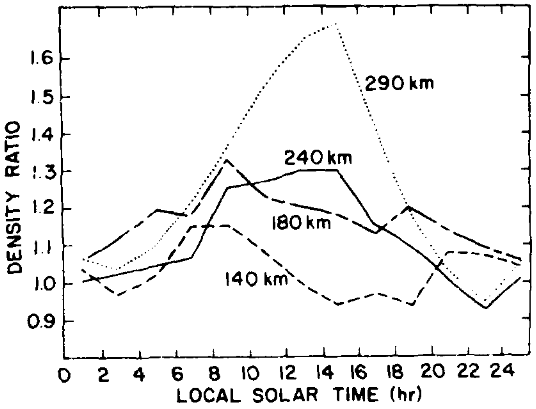

Figure 2. Average Ratio of the Measured Density to the Jacchia (1971) Model Prediction as a Function of Local Solar Time. The local time parameter for the model is taken to be local midnight in all cases, but all other parameters are handled in the manner prescribed in the model formulation. The data are binned at two-h intervals. Each curve includes all altitude increments within the 20 km band centered on the designated altitude (Sharp et al, 1978[38])

annual mean semidiurnal amplitude can lead to unrealistically small semidiurnal amplitudes, due to phase cancellation effects.

3.2 Atmospheric Gravity Waves

A few measurements of the total atmospheric density have been made using rocketborne falling spheres with accelerometers that are capable of making measurements with altitude resolution of 100 m. These measurements reveal a high degree of spatial structure in the measured density (see Figures 3 and 4). Figure 3 shows an example of the wave structure observed in the mesosphere and lower thermosphere using a recently developed accelerometer technique (Philbrick et al, 1978[34]). Small-scale wave structures that are consistent with gravity waves (see Figure 1) are observed to be superimposed on longer wavelength oscillations. The large-scale waves above 70 km altitude in Figures 3 and 4 are presumably due to a combination of large-scale gravity waves of tidal oscillations or possibly artifacts due to the atmospheric model used for comparison. The appearance of the small-scale waves, as shown in these figures, has been observed on all of the half dozen flights that could have detected such waves. Thus, they are expected to be present under most conditions. Figure 4b shows the temperature derived on the

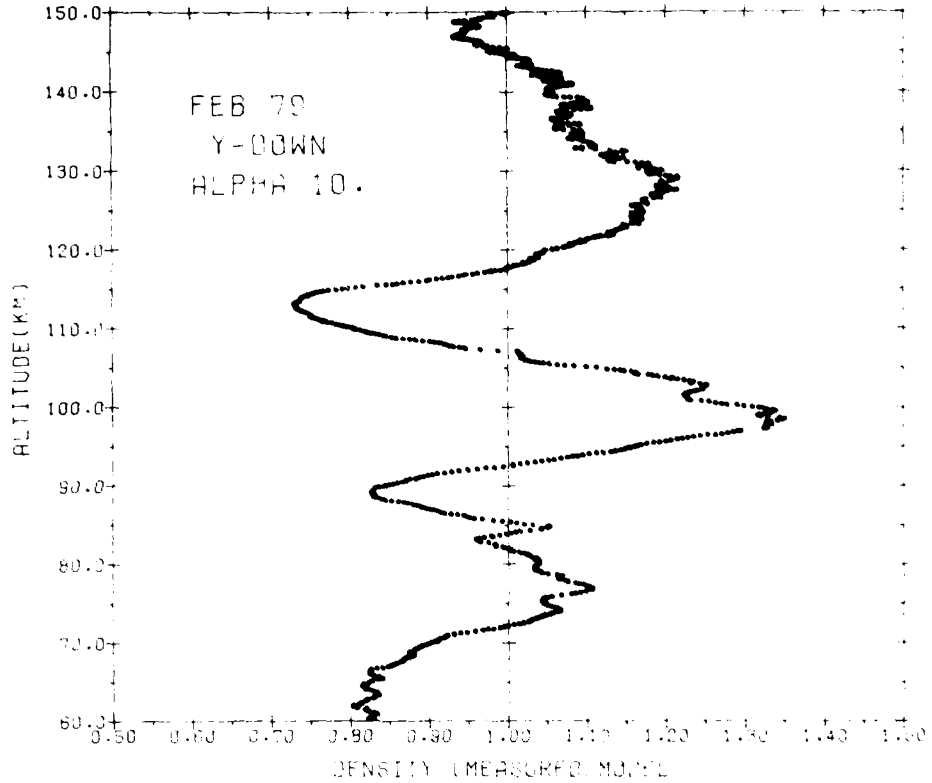

Figure 3. Density Measurements Made on 26 February 1979 are Shown as a Ratio to the USSA 76 Standard Model. Short wavelength (2-4 km) structure features are superimposed on longer-scale waves. The scatter of the measurement points at higher altitudes is due to the telemetry resolution of the data

basis of the density profile of Figure 4a and shows a high degree of vertical structure.

Figure 5 indicates the temporal dependence of the vertical structure (Philbrick et al, 1980[39]). This figure shows the results of density measurements made at Kwajalein Atoll for two sets of falling sphere flights. The larger waves are seen to be nearly stationary in space (that is, not propagating vertically) over periods of several hours. These measurements were accompanied by simultaneous measurements of the wind velocity that permits a calculation of the Richardson number

---

[39] Philbrick, C.R., Murphy, E.A., Zimmerman, S.P., Fletcher, E.J., Jr., and Olsen, R.O. (1980) Mesospheric density variability, Space Research XX:79-82.

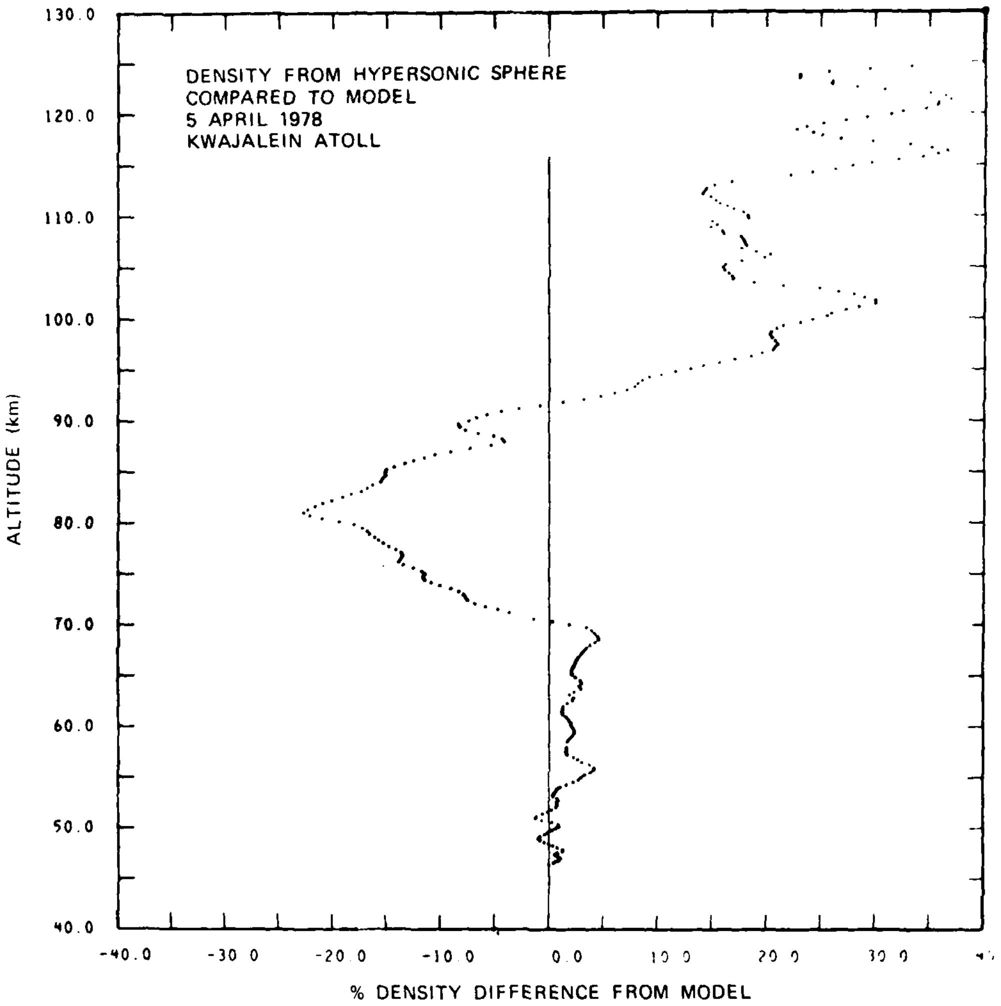

Figure 4a. Hypersonic Sphere Density Results from the Lincoln Laboratory, Analysis of the ALCOR Radar Data Compared to Model. Note the scale sizes of the vertical structure compared to the scales expected based on arguments presented in Figure 1 (Philbrick et al, 1978[34])

R_i. The results of this calculation are also shown in Figure 5. These plots show the scale sizes and the dynamically unstable regions ($R_i \leq 0.25$) due to the presence of wind shear. Negative values of the Richardson number exists in regions that are statically unstable because of the local density gradient.

In addition to these total density measurements, several rocketborne mass spectrometers have made measurements in the altitude range from 80 to 120 km.

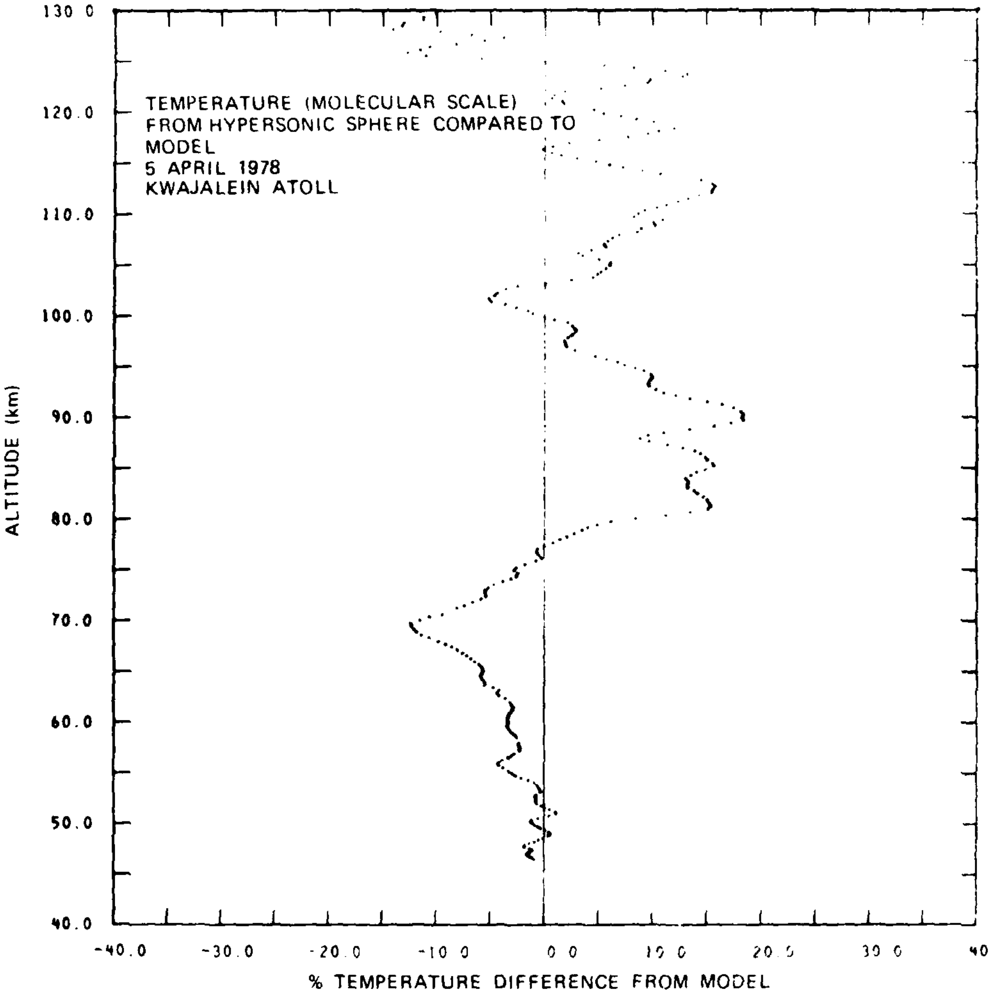

Figure 4b. Temperature from Lincoln Laboratory, Analysis of the Hypersonic Sphere Data Compared to Model (Philbrick et al, 1978[34])

Figure 6 shows an example of these measurements (Philbrick et al, 1978[34]), where vertical wave structures are apparent in the species profiles. The atomic oxygen profile reveals a substantial amount of spatial structure. Similar structure has been observed in most flights. Measurements of the vertical structure of atomic oxygen made at the White Sands Missile Range (WSMR) using resonant

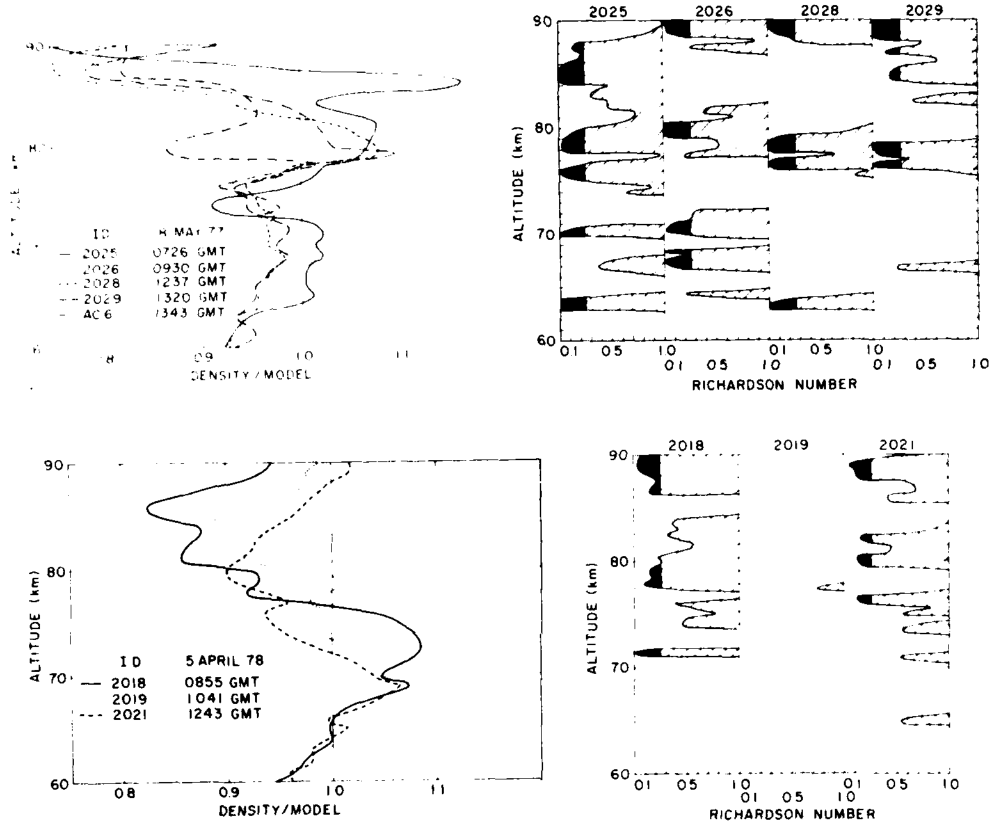

Figure 5. Density Measurements and Richardson Numbers for Falling Sphere Flights at Kwajalein Atoll on 18 May 1977 and 5 April 1978. (a) The density measurements are shown as a ratio to the Cole and Kantor tropical atmosphere for four Robin sphere flights and one accelerometer instrumented sphere (AC-6). (b) The Richardson numbers calculated from the temperature and wind measurements are shown for the range of values $0 < R_i < 1$ with the negative values plotted at $R_i = 0$. (Philbrick et al, 1980[39])

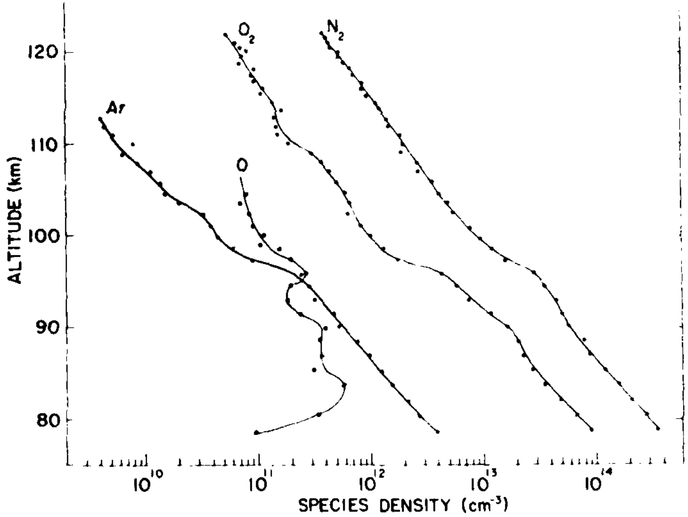

Figure 6. Species Densities vs Altitude Measured by the Mass Spectrometer on 23 January 1976 (Philbrick et al, 1978[34])

scattering of light indicates similar spatial structure (Figure 7, Howlett et al, 1980[40]).

Results obtained from a dynamic model of the mesosphere and lower thermosphere (Keneshea et al, 1979[41]) are compared in Figure 8 with profile measurements obtained on 20 November 1970. This model requires data on the atmospheric composition and temperature as a function of altitude, as well as the molecular and turbulent diffusion coefficients. The latter are determined from wind trail measurements. The substantial agreement between theory and measurements indicates the importance of considering the atmospheric dynamics. Recent improvements in the Schumann-Runge flux factor would produce less atomic oxygen in the model calculation and improve the agreement between the model and the measured density of this species. The agreement supports the conclusion that atmospheric dynamics can strongly influence the density profile of a minor species such as atomic oxygen in the 80 to 100 km region.

---

40. Howlett, L.C., Baker, K.D., Megill, L.R., Shaw, A.W. and Pendleton, W.R. (1980) Measurement of a structured profile of atomic oxygen in the mesosphere and lower thermosphere, J. Geophys. Res. 85:1291-1298.

41. Keneshea, T.J., Zimmerman, S.P. and Philbrick, C.R. (1979) A dynamic model of the mesosphere and lower thermosphere, Planet. Space Sci. 27: 385-401.

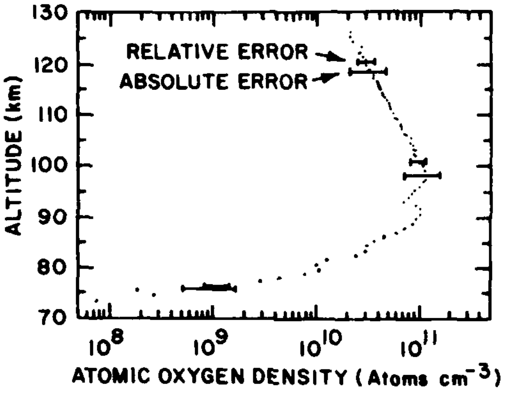

Figure 7a. Atomic Oxygen Density on Ascent Showing an Estimate of Relative and Absolute Errors (Three-sec running average with one point per sec shown) (Howlett et al, 1980[40])

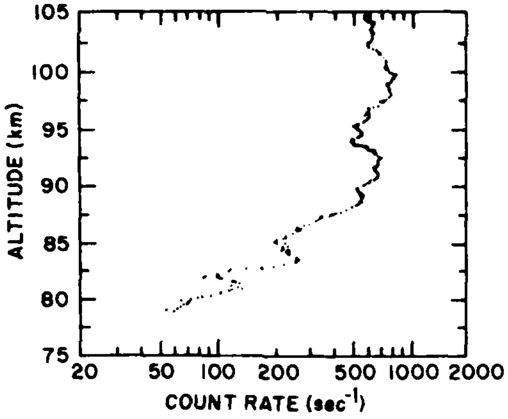

Figure 7b. High-resolution Ascent Data Showing Considerable Structure (One-sec running average with one point per 0.1 sec shown) (Howlett et al, 1980[40])

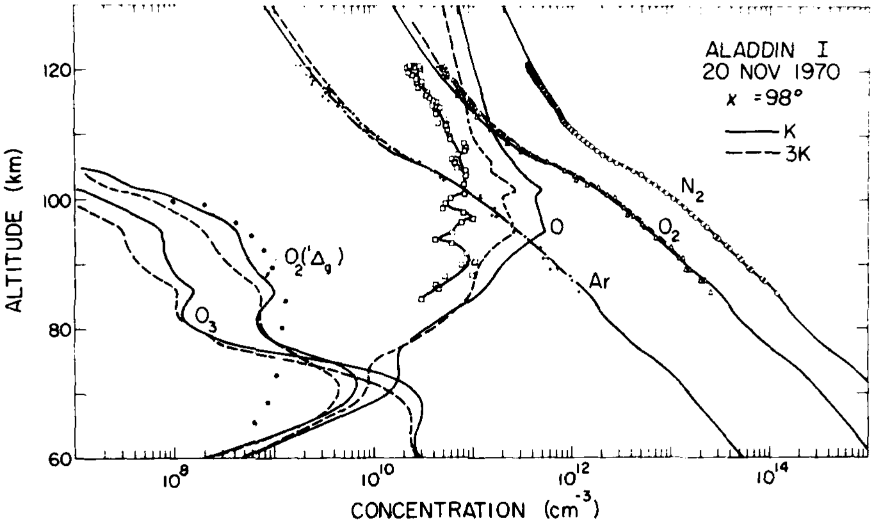

Figure 8. Comparison of Computed Species Profiles for Turbulent Diffusivities K and 3K (solid dashed curves) With Measured Profiles for O (squares), O_2 (triangle), N_2 (circles), Ar (crosses), and $O_2(^1\Delta_g)$(dots)

At higher altitudes, satellite measurements show wave-like variations that are thought to be due to gravity waves. In Figure 9, measurements made during flights of the S3-4 satellite (McIssac, 1980[42]) reveal the presence of these waves with horizontal wavelengths of hundreds of km. These waves are frequently observed at high altitudes and are always present for disturbed periods ($K_p \geq 4$). The structure is strongly correlated with the auroral region and probably associated with pressure gradients created by momentum sources or localized heating in the lower thermosphere or upper mesosphere.

The nature of these waves is shown more clearly in the measurements made using the Nace instruments on flights of the AE-C satellite (Reber et al, 1975[43]). In Figure 10 the wave structure is clearly revealed. The authors of this study (Reber et al, 1975[43]) concluded from their analyses of the spatial structure for two orbits that: "This structure exhibits (1) scale sizes from a few tens of kilometers to several hundreds of km, (2) molecular nitrogen density amplitudes of the order of 5-15%, argon amplitudes about half of N_2 amplitudes and generally 180° out-of-phase with the N_2 and Ar, ... The neutral data are qualitatively consistent

---

[42] McIssac, J.P. (1980) Private communication.

[43] Reber, C.A., Hedin, A.E., Pelz, D.T., Potter, W.E., and Brace, L.H. (1975) Phase and amplitude relationships of wave structure observed in the lower thermosphere, J. Geophys. Res. 80:4576-4580.

S3-4 NEUTRAL DENSITY MEASUREMENTS

Particle Flux Accumulator Experiment

NEUTRAL DENSITY PHENOMENA – Atmospheric Waves

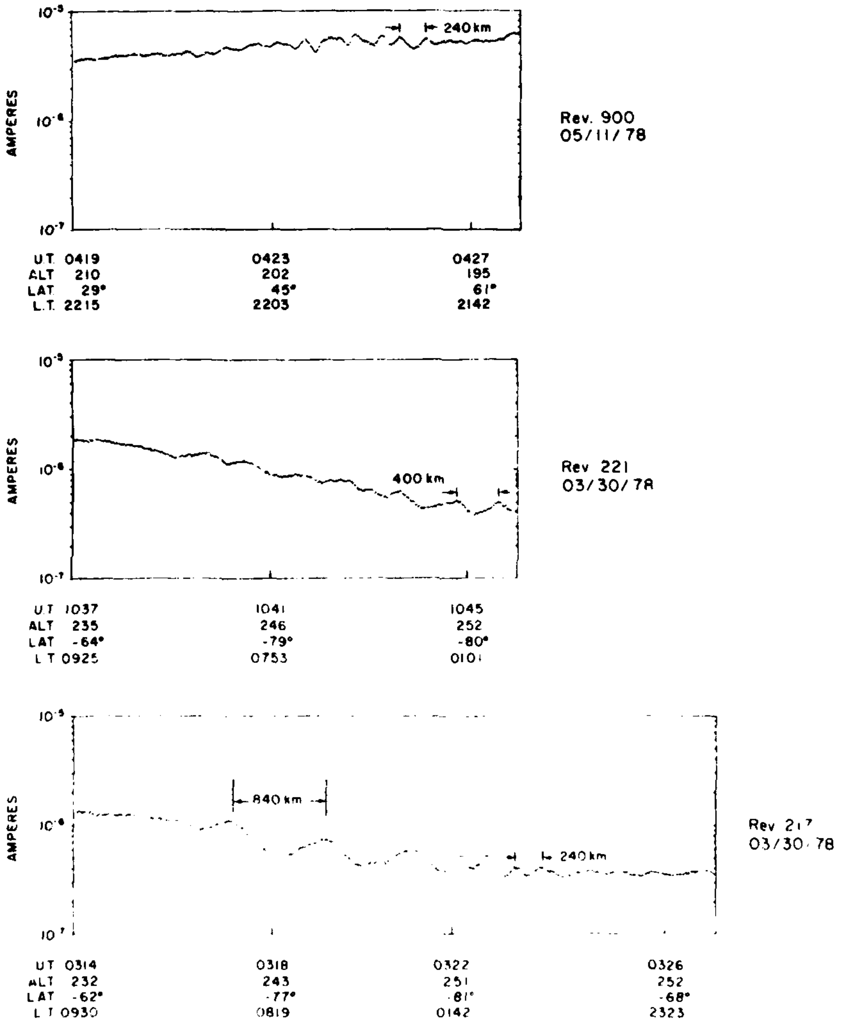

Figure 9. S3-4 Neutral Density Measurements – Particle Flux Accumulator Experiment Neutral Density Phenomena – Atmospheric Waves (McIssac, 1980[42])

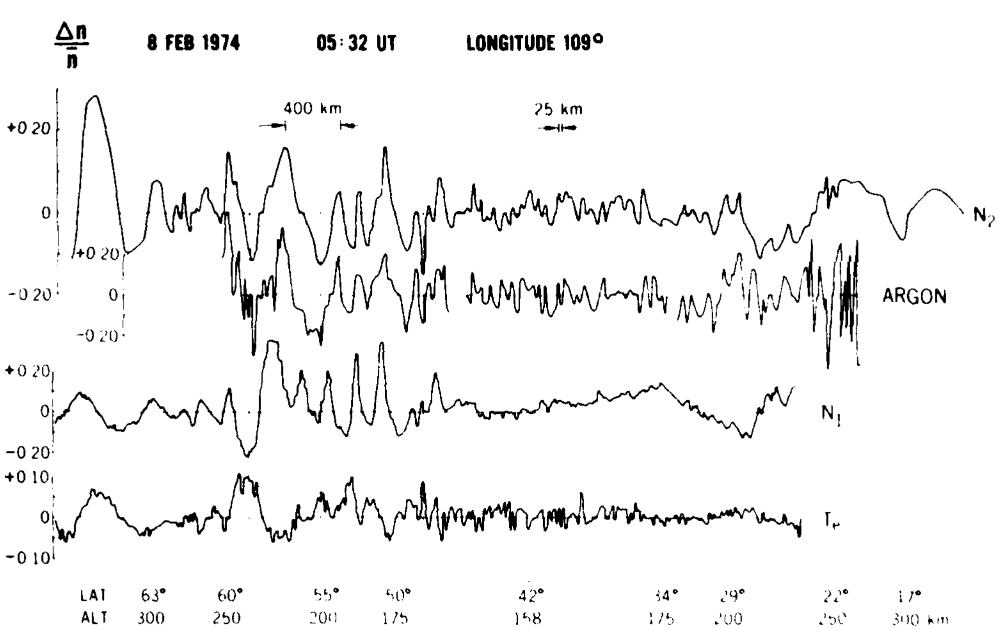

Figure 10. The Structural Variations of Molecular Nitrogen, Argon, Total Ion Density, and Electron Temperature. The relative scale sizes along the satellite trajectory are shown, and again the vertical lines emphasize the phasing between parameters. The entire data set was obtained in 14.7 min at a satellite speed of 8.6 km^{-1} (Reber et al, 1975[43])

with a simple picture of wave-like density enhancements in the major species nearly in phase with the vertical component of the perturbation velocity, ... "

Later analysis of the OSS data obtained on the AE-C satellite (Potter et al, 1976[44]) has shown the amplitudes of the waves increase at the high-latitude auroral regions, indicating that the waves were apparently generated by magnetic storm energy deposition and propagate both northward and southward from the region of the auroral electrojet. An example of the OSS results are shown in Figure 11. It is expected that similar wave structure would appear in the infrared radiation due to CO_2 from these regions, as the spatial variations in the CO_2 that result from mass motions are expected to be similar to that of Ar.

The momentum source is one of the features of the thermosphere that manifests itself in significant high-latitude structure during periods of enhanced geomagnetic activity. The momentum source manifests itself by a pressure gradient due to momentum transfer to neutrals from ions accelerated by electric fields.

---

[44] Potter, W.E., Kayser, D.C. and Mauersberger, K. (1976) Direct measurements of neutral wave characteristics in the thermosphere, J. Geophys. Res. 81: 5002-5012.

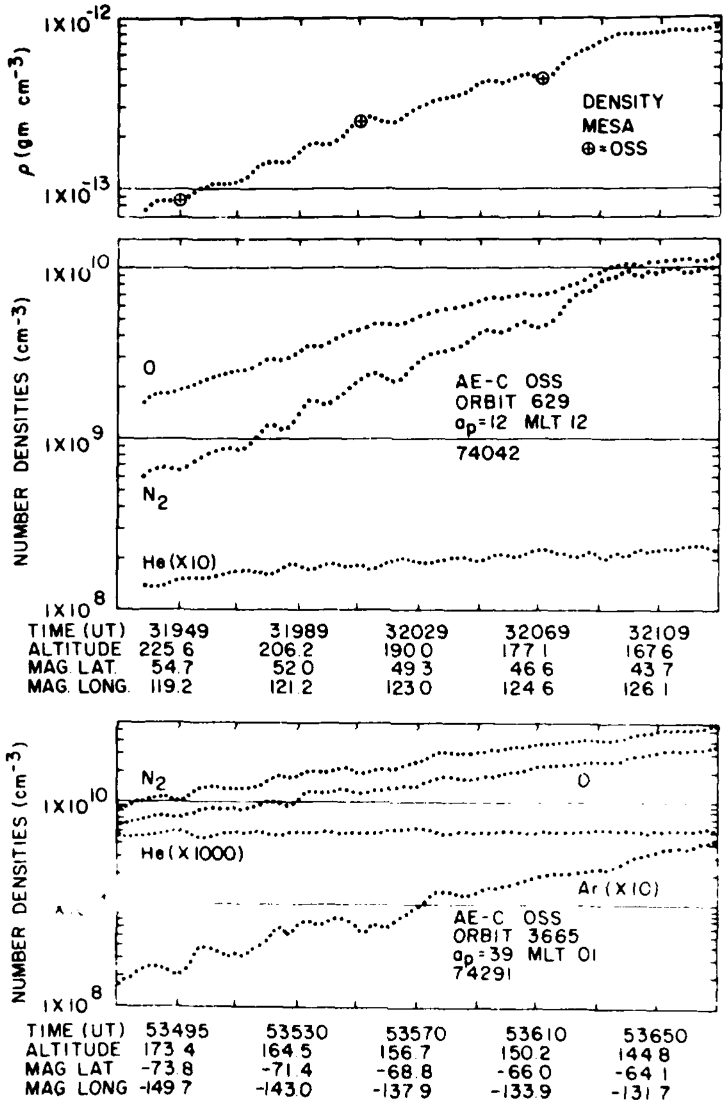

Figure 11. The Center and Bottom Panels Show OSS Neutral Number Densities for Two Elliptical Orbits. The mass dependent wave structure is evident, as is the out-of-phase behavior of He. The top panel shows the total Mesa mass density from orbit 629, that closely follows the OSS N_2 number density in the center panel. The circled pluses shown in the top panel are mass densities calculated from OSS constituent number densities. Altitudes are given in km. The (O) densities represent the total atmosphere oxygen. The universal time (UT) is given in sec after the start of the day

Perturbations in the structure of the neutral atmosphere in narrow latitude bands near the dayside polar cusp have been measured aboard the S3-1 and Esro 4 satellites (Trinks et al, 1978a[45]). Examples of these perturbations are shown in Figures 12 to 14. Figures 12 and 13 present measurements made aboard the S3-1 satellite. These measurements show fluctuation amplitudes of as much as a factor of two in species concentrations and with spatial dimensions of approximately 300 km. Figure 14 presents the measurements made aboard the Esro 4 satellite and indicate similar magnitudes and extents. Trinks et al, (1978b)[46] discuss these measurements and suggest that thermospheric winds driven by "momentum sources" associated with ion convection are the predominant cause for these disturbances. The narrow spatial structure and in phase response of all species are characteristics associated with the momentum source. These effects are generally superimposed on the thermosphere expansion changes caused by Joule heating. Momentum source disturbances probably generate waves which are propagated to lower latitudes.

3.3 Ionospheric Response to Geomagnetic Activity

Ion densities have been measured on a number of satellite flights. The effects of increased geomagnetic activity on the ionic concentration can be seen by comparing Figures 15 and 16. Figure 15 shows ion species concentrations during a quiet period and displays the typical structure of the F layers. In Figure 16 the normal F_2 layer at high latitudes is severely changed during a period of high geomagnetic activity ($K_p = 6$). In the disturbed region there is a large amount of spatial structure of scale sizes of tens of km. The O^+ is decreased in the F_2 peak due to the effect of the electric fields that increase the loss rate of the ion molecule reactions with N_2 and O_2. The substantial increase in the N_2^+ is due to enhanced ionization by the precipitating particles.

3.4 Summary

Measurements of the total density below 90 km reveal substantial structure with scale sizes that are in agreement with theoretical predictions of gravity wave theory and tidal theory. At higher altitudes gravity waves are also apparent but with longer wavelengths (tens of km). Satellite observations reveal wave structure in the species concentrations with scale sizes from tens of km to several hundred

---

[45] Trinks, H., Mayr, H.G. and Philbrick, C.R. (1978a) Momentum source signatures in thermospheric neutral composition, J. Geophys. Res. 83:1641-1646.

[46] Trinks, H., Offerman, D., von Zahn, U. and Steinhauer, C. (1978b) Neutral composition measurements between 90 and 220 km altitude by rocket-borne mass spectrometer, J. Geophys. Res. 83:2169-2176.

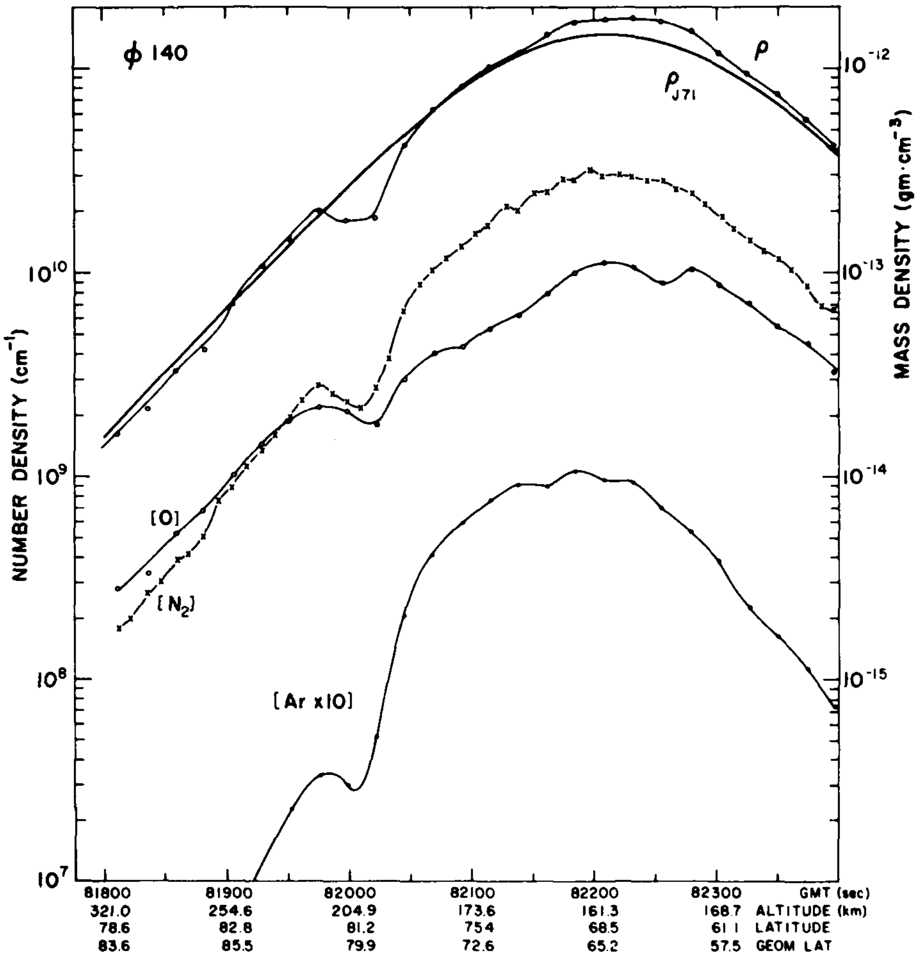

Figure 12. Perturbation in the Structure of the Atmospheric Mass Density and Species Concentrations Measured by Mass Spectrometer During S3-1 Satellite Flight

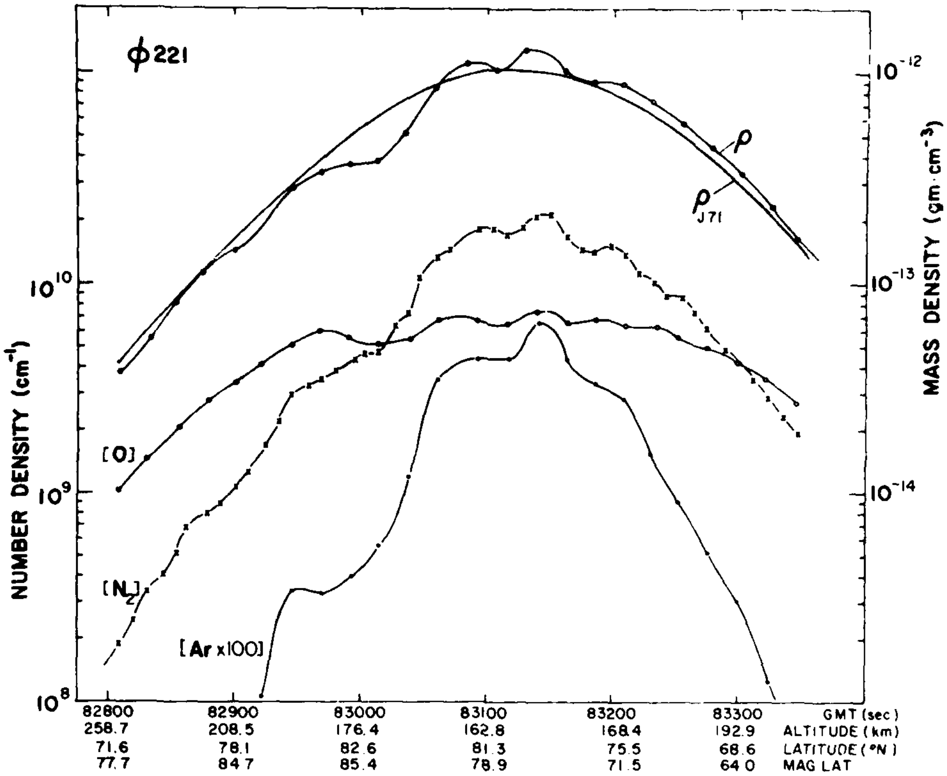

Figure 13. Severe Perturbation in the Structure of the Atmospheric Mass Density and Species Concentrations Measured by Mass Spectrometer During S3-1 Satellite Flight

kilometers. The description of these small-scale features of atmospheric variations would require a great deal of knowledge concerning the sources of the particular disturbance, as well as detailed 3-D calculations of atmospheric motion. This is not feasible at the present time and one must rely on a statistical description of the magnitude, spatial scale-size distribution, and frequency. With such a description it should be possible to evaluate the variability of the resultant infrared radiance.

Figures 17 and 18 give indications of the scales and amplitudes of waves and other structure features that have been observed in the upper atmosphere. In Figure 17 the range of theoretically predicted scale sizes for gravity waves (Hines, 1960[11]) and tidal oscillations (Forbes, 1978[9]) are shown for both the vertical and horizontal structure. On the outside edge of the figure, several of the structure scales that have been measured (most are from examples shown earlier in this

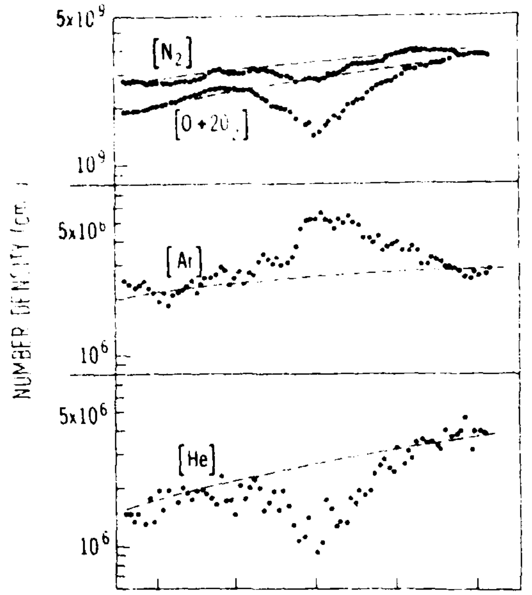

UT (7 Apr 1974)	10 06		10 11		10 16
LST (hours)	23.7	21.8	12.5	12.2	12.1
HEIGHT (km)	208.7		207.4		210.5
GEOGR LAT N	79	88	81	71	61
GEOGR LONG E	204	176	35	31	29

Figure 14. Ambient Number Densities of Molecular Nitrogen, Total Oxygen, Argon, and Helium from the Esro 4 Gas Analyzer vs Universal Time, Height, and Geographic Coordinates. The disturbance is centered at 1011 UT (Trinks et al, 1978a,[45] 1978b[46])

chapter) are indicated. There is satisfying consistency between the scales predicted for gravity waves and tidal oscillations and the structure scales that have been measured in the atmosphere. One of the open questions is the minimum scale size to be considered for localized heating, such as auroral arcs and precipitation sources. It may be that the smaller scale sizes needed for consideration in infrared radiance characterization are determined by these excitation mechanism. In Figure 18 the altitude distribution of the measured scale sizes are given for a number of cases from the results discussed in this report. The amplitude of the structure is indicated by the length of the plotted lines. The interesting point to notice is that at low altitudes, the characteristic scale sizes are typically one to a few km and amplitudes are a few percent. In moving to

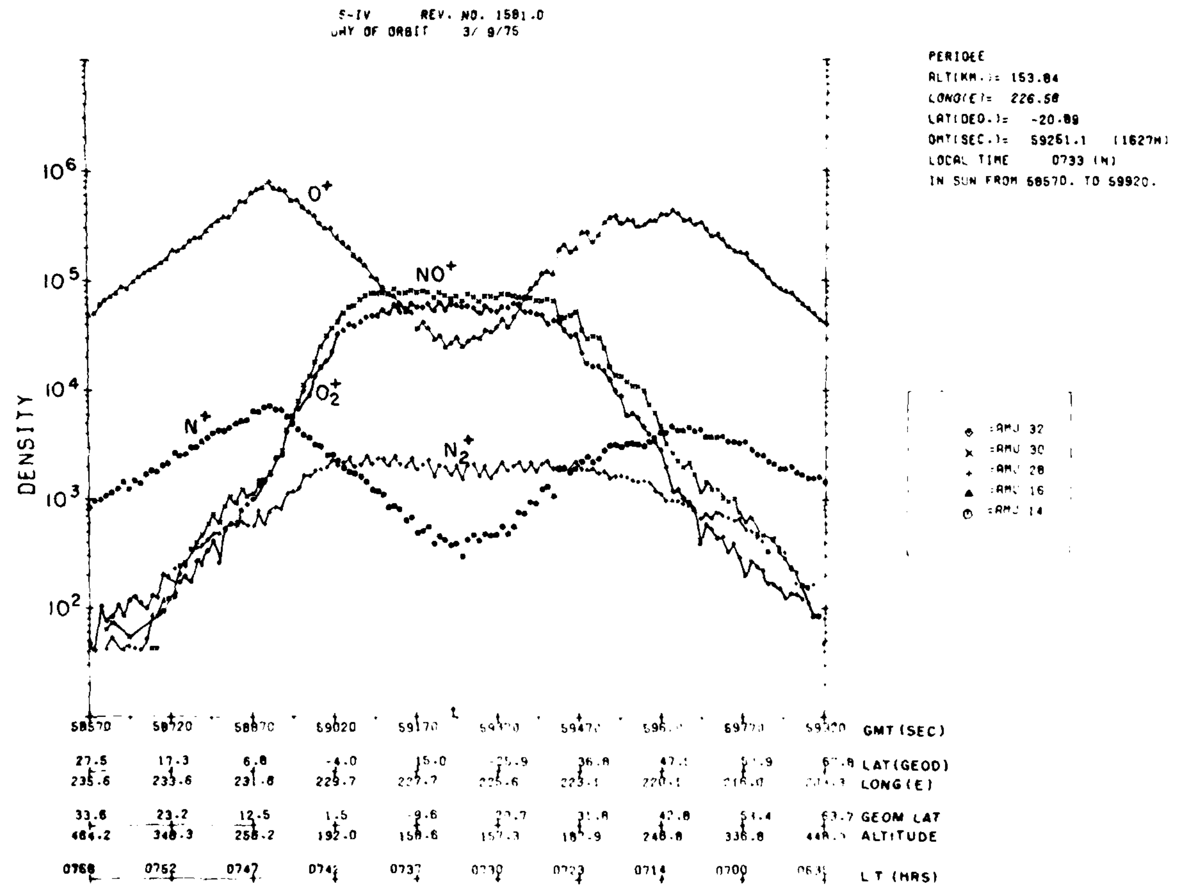

Figure 15. Ion Species Concentrations Measured by MS-IV Satellite During Quiet Magnetic Conditions

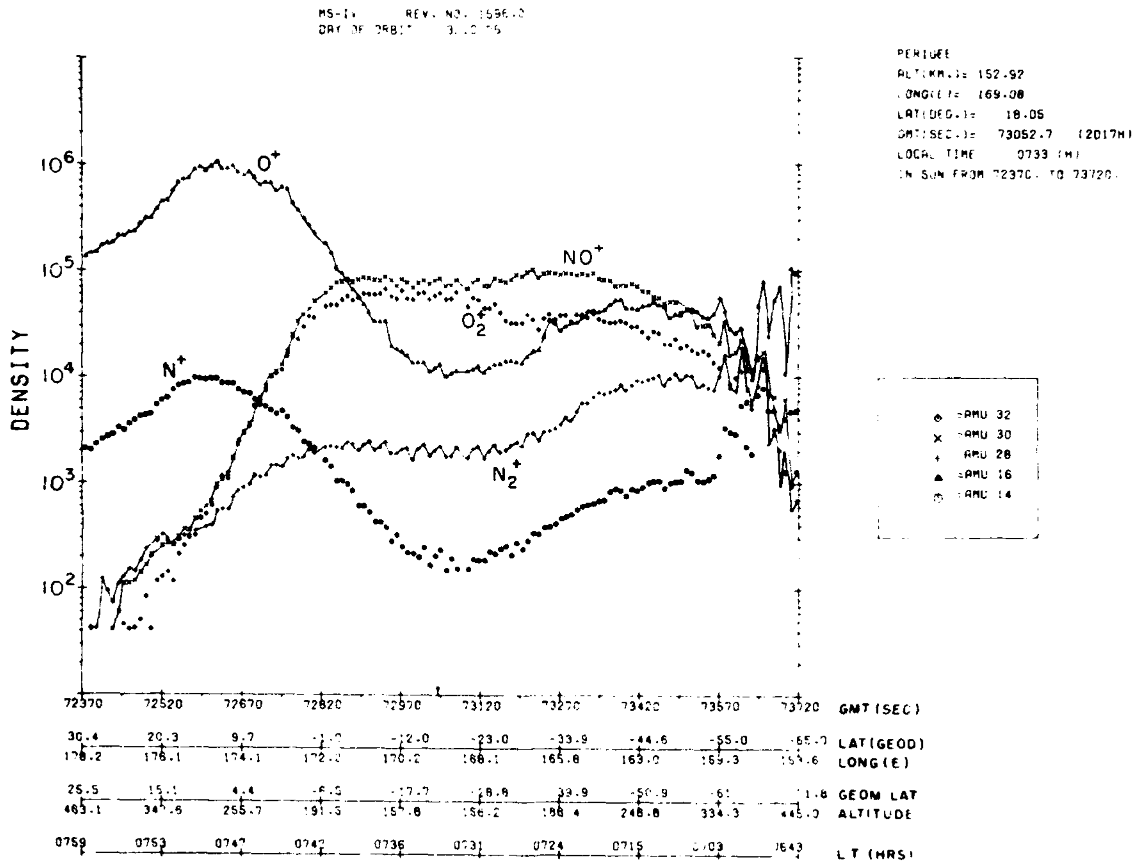

Figure 16. Ion Species Concentration Measured by Instruments Aboard MS-IV Satellite During Disturbed Magnetic Conditions (K_p = 6)

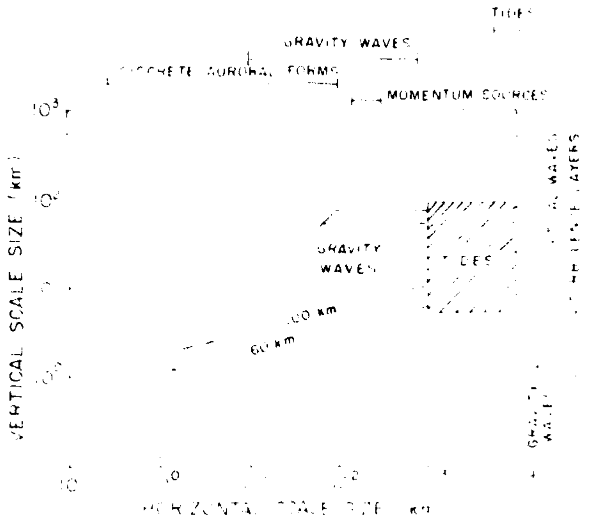

Figure 17. Theoretical Scale Sizes for Gravity Waves and Tidal Oscillations. Outside edges indicate measured scale sizes.

higher altitudes the amplitude and scale size both increase. While it is certainly not a complete picture, it does present an idea of the typical behavior under moderately disturbed atmospheric conditions. These considerations apply to the total density of the atmosphere. The structure and variability of an individual minor species may be substantially greater.

From this review, we conclude that substantial variations occur in the density distribution of the infrared radiating species of the atmosphere, both spatially and temporally. This chapter has only discussed the variations and scales associated with the species concentrations, but the excitation processes may be more important to the radiance under some circumstances. At present it is difficult to determine the full impact of these variations on the resultant infrared radiance. It can be inferred, for example, that the density of CO_2 at 150 km would be expected to increase by more than a factor of ten under high latitude geomagnetic heating. With the calculations discussed elsewhere in this report and with the data presented here these questions can begin to be answered.

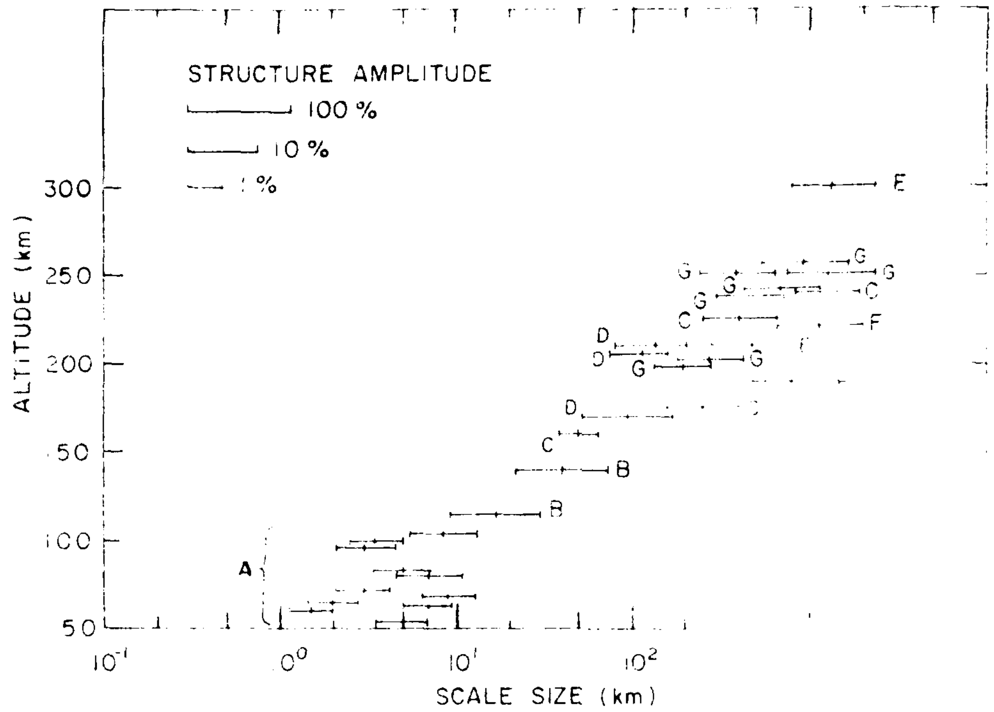

A. Rocketborne accelerometer, Philbrick et al, 1978a[47]
B. Rocketborne mass spectrometer, Trinks et al, 1978b[46]
C. AE-C satellite mass spectrometer, Reber et al, 1975[43]
D. AE-C satellite mass spectrometer, Potter et al, 1976[44]
E. S3-1 satellite mass spectrometer, Philbrick, 1976[48]
F. S3-1 satellite mass spectrometer, Trinks et al, 1978a[45]
G. S3-4 satellite density gauge, McIssac, 1979[42]
H. S3-1 satellite mass spectrometer, Philbrick, 1980[49]

Figure 18. Altitude Distribution of Measured Scale Sizes from Indicated Sources. Amplitude of structures are indicated by length of plotted line. The rocketborne data show vertical structure and the satellite shows horizontal structure

---

[47] Philbrick, C.R., Faire, A.E., and Fryklund, D.H. (1978a) Measurements of Atmospheric Density at Kwajalein Atoll, 18 May 1977, AFGL-TR-0058, AD A054 784.

[48] Philbrick, C.R. (1976) Recent satellite measurements of upper atmospheric composition, Space Research XVI:289-295.

[49] Philbrick, C.R. (1980) Private communication.

4. ATMOSPHERIC BACKGROUND CLUTTER ANALYSIS

Preliminary calculations (Titus and Anapol, 1979[50]) of the noise or clutter produced by fluctuations in the CO_2 radiation have been made using a model based on satellite mass spectrometer measurements of density variations in the upper atmosphere combined with estimates of the mean radiance along a path obtained from the High Altitude Radiance Model. CO_2 is the dominant radiator throughout much of the infrared, but it is one of the most difficult molecules to measure using mass spectroscopy. Because of this difficulty, CO_2 density data at higher altitudes are almost nonexistent and, therefore, Ar data (Figure 19(a)) was taken to be approximately representative of CO_2. As discussed in Section 3, Reber et al (1975)[43] have published spatial density variations for AR at high altitudes (see Figure 10). Using the assumption that the radiance is directly proportional to molecular density, the power spectrum (PSD) of the radiance spatial structure was derived from these data. The correlation length is found to be approximately 10 km and the roll-off of the PSD is f^{-2} (Figure 19(b)) where f is the spatial frequency. Satellite ionosphere density (SRI wideband experiment) measurements at these altitudes and accelerometer and calorimeter measurements appear to confirm these values. The large-scale correlation length of the AE-C mass spectrometer data is approximately 450 km. This length is corroborated by the SPIRE data and S3-1 mass spectrometer measurements.

The impact of radiance structure on a sensor inbedded in the limb is as shown in Figure 19(c). A shell model of radiance is constructed at correlation intervals and the power spectrum calculated for each intersection of the line-of-sight and a shell. The power spectrum is integrated at each range point to obtain the mean square clutter in the sensor passband and these values summed along range to obtain the integrated mean square clutter noise.

Measurements during aurorally active conditions exhibit much larger density variability and smaller correlation lengths. In addition, the fluctuations of Ar were observed to be much larger than those of N. This mass dependence translates into a spectral dependent model of clutter since each species will behave differently. Large radiance enhancements during aurora have been measured at shorter wavelengths and are theoretically expected at longer wavelengths. Therefore (and not unexpected), the impact of the disturbed upper atmospheric conditions will be more severe than the quiescent atmosphere.

---

[50] Titus, J. and Anapol, M. (1979) Private communication.

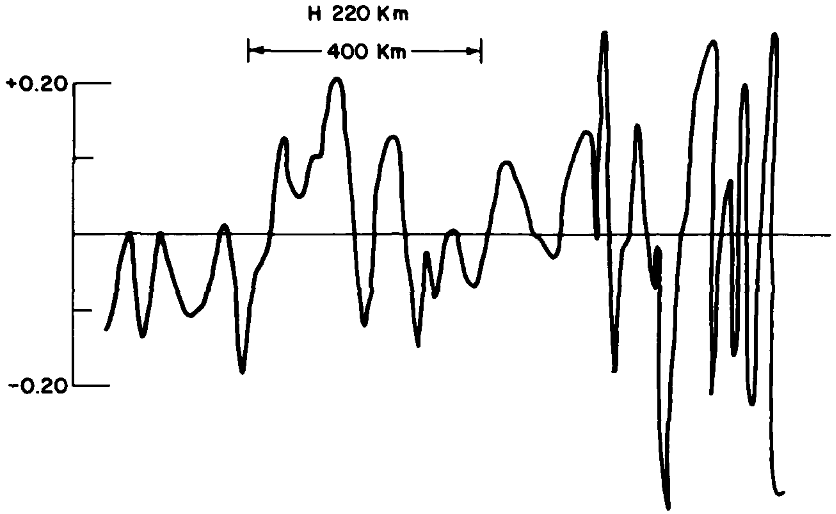

(a) Argon Spacial Structure

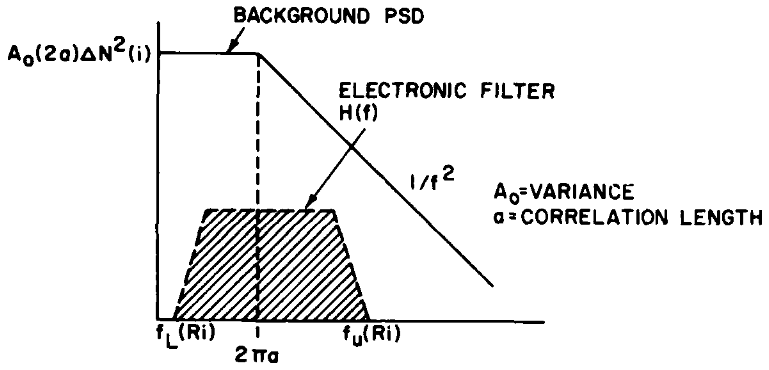

(b) Atmosphere Background PSD

BACKGROUND CLUTTER

$$\left\{\sum_{i=1}^{H}\left[\int_{f_L}^{f_u} PSD(f,i)\,H(f,R_i)\,df\right]\right\}^{1/2}$$

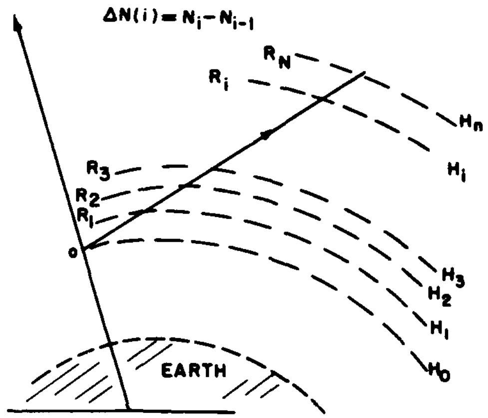

(c) Background Shell Model

Figure 19. Atmosphere Background Clutter Analysis

5. AURORAL EXCITATION OF INFRARED RADIATORS

Even if the concentration and density distribution of each of the potential infrared emitters were known, the radiance at high latitudes may be difficult to predict because of the fluorescence and direct collisional excitation sources together with localized temperature enhancements. In this section a brief discussion will be given of several sets of information that are related to the energy sources that input to the upper atmosphere. The energy input in the auroral zone may be studied by examining the ionospheric response, particularly the N_2^+ enhancement due to particle ionization and the O^+ depletions due to the electric field produced increases in ion molecule loss reactions. The visible radiation from all-sky cameras on DMSP satellite photographs provide an excellent means of characterizing the location, structure, and intensity of energy deposition. Ground-based video recording systems have also been used to study the auroral characteristics. A recent satellite ultraviolet photometer, Huffman et al, (1979),[51] has also provided nadir looking data on the ultraviolet emission excited in the auroral zones. In Figure 20 measurements of the radiation at 155 nm (the Lyman-Birge-Hopfield band of molecular nitrogen), from a 20° portion of the auroral oval showing arcs and continuous aurora, are presented.

An aurora is a region of considerable variability of luminosity. In spatial extent it may vary in width from the order of km to hundreds of km, and in length in thousands of km. The structure is very heterogeneous and, thus, the aurora is potentially a significant source of fluctuating infrared radiation. Examples which show the variety of auroral forms that may be encountered are shown in Figure 21, from the DMSP satellite system operating in the infrared. The land mass outlined by the lights is the eastern part of the United States.

In addition to the well-known visible aurora, typified by the DMSP photographs, we may have the occurrence of midlatitude auroral red arcs during periods of high magnetic activity. These occur to the south of the southern extension of the visible aurora, Figure 22, (N. B. S., 1962[52]) have widths of the order of several hundred km, and extend for thousands of km in longitude. These arcs are characterized by a predominance of the 630 nm O line. Their altitudes are typically above 300 km.

In Figure 23 ion concentrations are shown for two satellite flights through auroral disturbances. In both cases the aurora were Class III. The ion concentrations display the high degree of irregularity to be expected under such circumstances.

---

[51] Huffman, R. E., LeBlanc, F. J., Larrabee, J. C. and Paulsen, D. E. (1979) Satellite Atmospheric Radiance Measurements in the Vacuum Ultraviolet, AFGL-TR-79-0151, AD A078 628.

[52] N. B. S. (1962) Auroral arcs in mid-latitudes, National Bureau of Standards Technical News Bulletin 46:42-46.

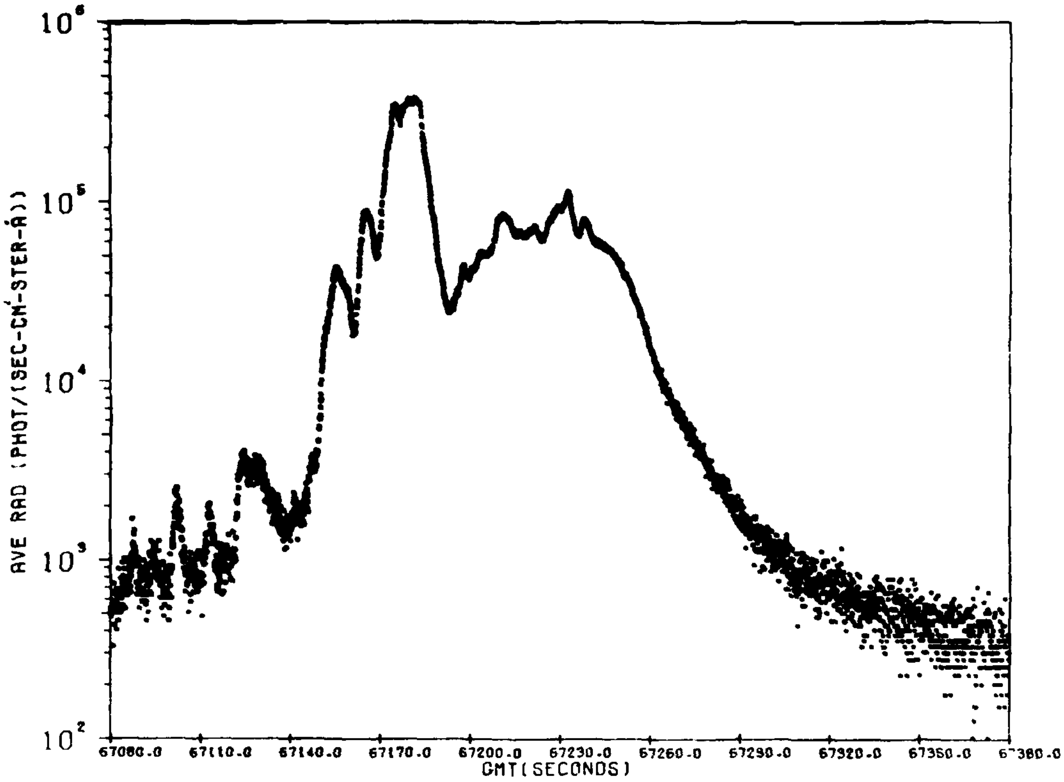

Figure 20. Radiation at 155 nm (Lyman-Birge-Hopfield) for a 20° Portion of the Auroral Oval

5.1 Application of Visible Monochromatic Auroral Imaging Data for Modeling Infrared Radiance

Effective design of sensitive infrared sensors operating in the limb viewing mode requires a statistically significant data base on the auroral infrared earthlimb background. Research that has been performed under the DNA/AFGL auroral measurements program has shown that there are strong auroral emissions near 2.7 and 4.3 μm (Stair et al, 1981[5]). It is possible to develop, to first order, a comprehensive 2.7 and 4.3 μm earthlimb model that is based on an existing all-sky TV data base. The TV data base includes approximately 200 hours of all-sky multispectral image intensified TV imaging data of aurora and airglow that have been taken and stored on video tape in the time period 1972 through 1977. Methods for modeling (blue red input model, BRIM) infrared emissions at 2.7 and 4.3 μm on the basis of ground-based photometric measurements of the aurora in the spectral regions blue (4278A) and red (6300A) have recently been developed and verified against infrared data that were obtained simultaneously via rocketborne sensors.

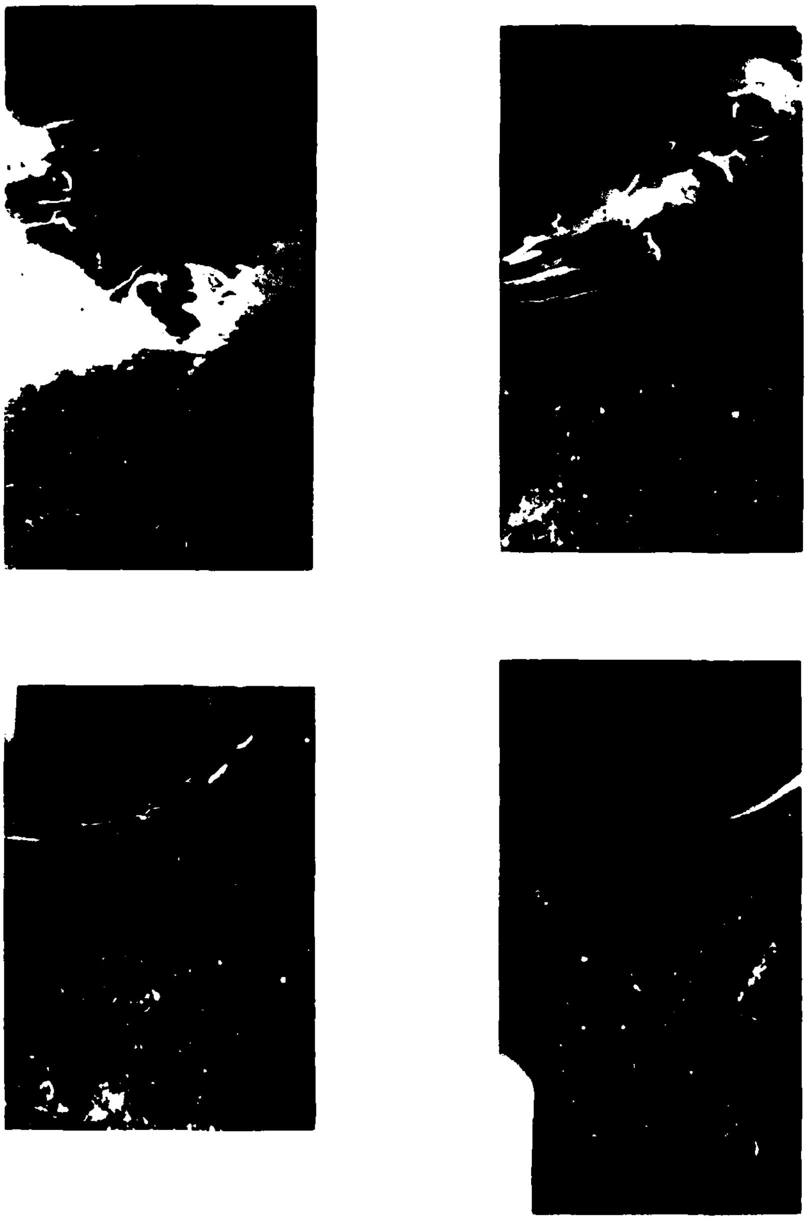

Figure 21. DMSP Infrared Photographs of Various Auroral Forms

Figure 22. The Red Arc (shaded region) Lies South of the Southern Extension of the Visible Aurora (_)

In this section the use of the BRIM capability to construct images of the infrared earthlimb radiance from successive pairs of blue and red all-sky TV images is discussed. The images are obtained at a rate of once every 15 sec or faster. The spatial resolution of the TV is such that structure on the scale of several km may be resolved in the radiance images. The all-sky TV coverage has a zenith full cone angle of 160°. This is extensive enough so that images of horizontal extent of up to 700 km and tangent altitude from 40 to 140 km may be constructed. Spatial power spectral densities (PSDs) may be obtained from the images and temporal PSDs may be obtained from a series of images.

Methods inferred from the work reported by Rees and Luckey (1974)[53] may be used to approximately construct an energy deposition profile $q(z,t)$ from the TV brightness data measured in narrow spectral bands in the blue (4278A) and in the red (6300A) spectral region. The "blue" data $4\pi I_B(t)$ are proportional to the height integrated energy deposition and the ratio I_B/I_R of the blue to red may be associated with the altitude where q is a maximum if one assumes that the energy dependence of the incident electrons takes the form $\phi = \phi_0 E e^{-E/a}$. Kumer (1977)[54]

---

[53] Rees, M.H. and Luckey, D. (1974) Auroral electron energy derived from ratio of spectroscopic emissions, J. Geophys. Res. 79:5181-5186.

[54] Kumer, J.B. (1977) Further Evaluation of ICECAP Auroral 4.3 μm Zenith Radiance, Haes Report No. 57 DNA 4260F.

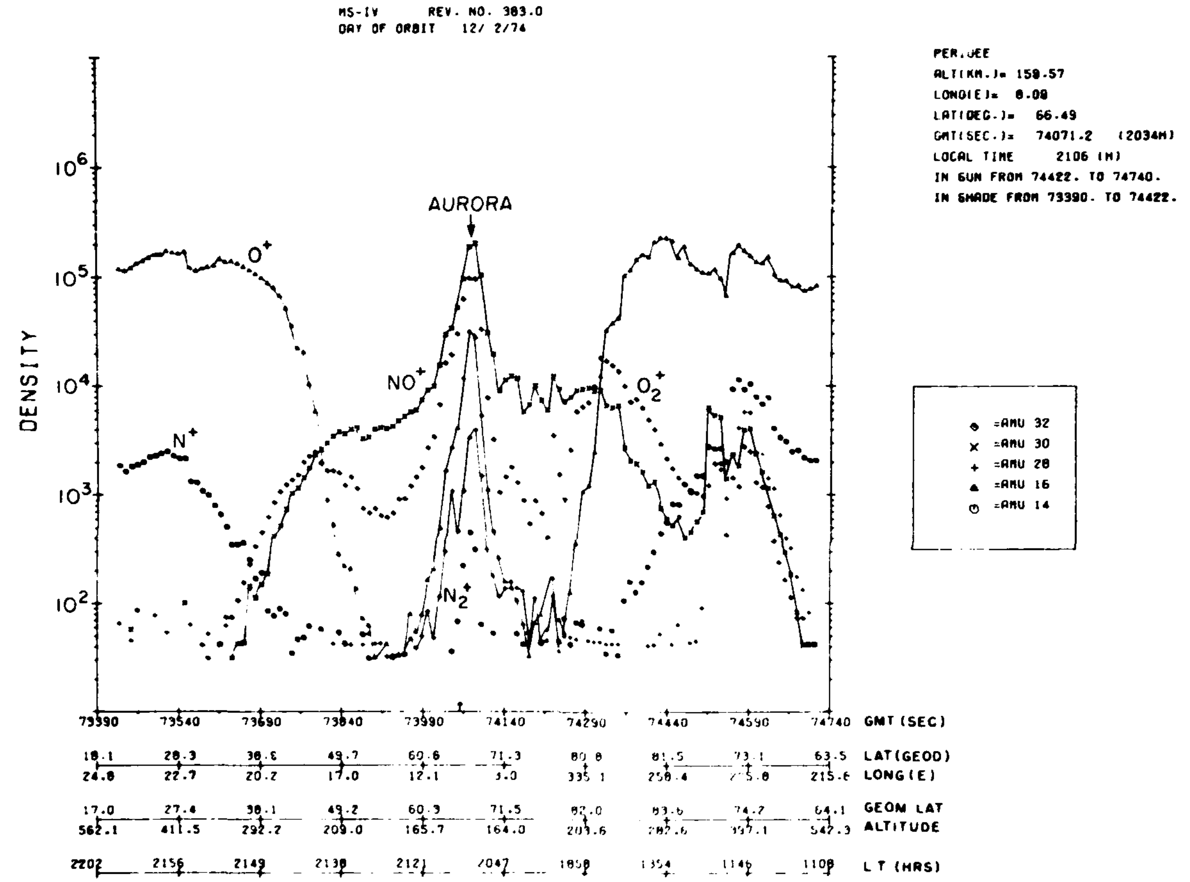

Figure 23. Ion Species Concentrations Measured by Instruments Aboard MS-IV Satellite During Auroral Activity

discussed in detail the BRIM method for approximately constructing a deposition profile q(z, t) from the blue and red brightness data. Examples of the excellent agreements between the up and down leg BRIM calculations for 4.3 μm zenith radiance and the data obtained in the case of the an auroral event of 25 February 1974 are shown on Figures 24 and 25. Ground-based photometric red and blue auroral data taken at the point of up-leg and downleg penetration at 80 to 110 km are input to the BRIM model.

The goal is to use a series of TV frames of blue data $4\pi I_B$ to generate a dynamic image of the corresponding infrared earthlimb radiance as it would appear when viewed from a satellite at some considerable distance from the earth. Line-by-line (or selected line) digitization of auroral images and image sequences is accomplished with a system which incorporates a controller that selects the proper TV frame, a digitizer, and an output couple to transfer the digital data stream to digital magnetic tape.

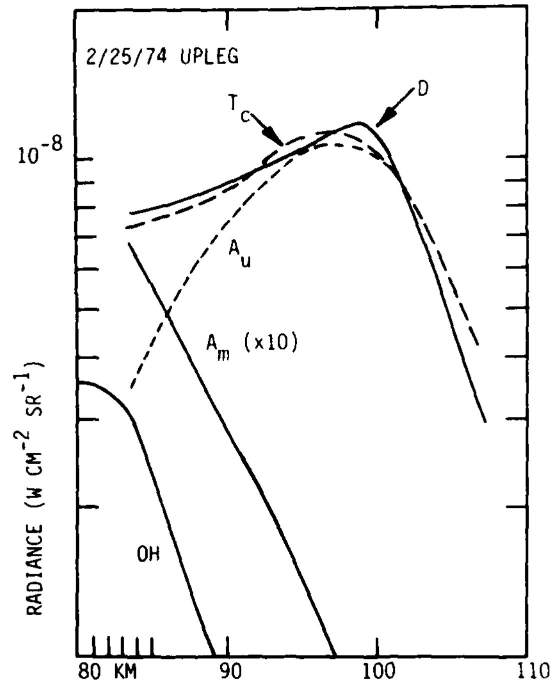

Figure 24. 25 February 1974 Upleg 4.3μm Zenith Radiance Data (curve D) are Compared With Curves A_u, the BRIM Calculation for the Auroral Component of Zenith Radiance; OH, the Calculated Component Due to Vibration Transfer from OH^+; A_m(x10), the Ambient Thermal Component Multiplied by a Factor 10 So That It is on Scale; and T_c, the Sum OH + A_u + A_m

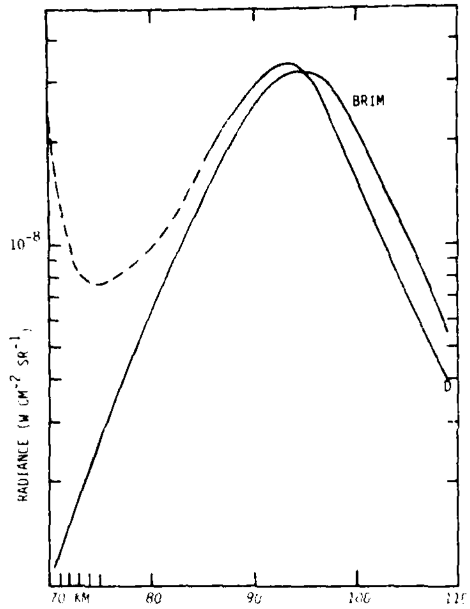

Figure 25. A Comparison of the 25 February 1974 Downleg Data (curve D) and Calculations (curve BRIM) Based on Our BRIM Model

To date Kumer and associates have developed software for the calculation of 2.7 and 4.3 μm earthlimb radiance from digitized blue and red zenith viewing all-sky TV data. Due to the lack of mass digitization of the TV data base at this time a version of the simulated TV data has been utilized to test the software. In this simulation of the earthlimb, radiance is calculated along 51 lines-of-sight with tangent altitude 110 km. The middle line-of-sight passes directly over the zenith of the TV station. The surface projection of this line-of-sight runs from magnetic northwest to southeast and is 30° magnetic south of due magnetic east. The lines-of-sight are parallel, 2 km apart, and tangent at 110 km altitude.

The earthlimb radiance calculations are performed on 50 pairs of simulated blue/red digitized TV data frames. These pairs of frames are spaced in time by 20 sec and thereby define an interval $0 < t < 16.67$ min. The first pair was generated from scanning photometer data. This initial pair is considered to represent a steady-state condition that had persisted for many min prior to $t = 0$ min.

At $t = 0$ it is assumed that a multiple arc structure appears in the field of view (FOV) and commences to move across the FOV in the positive direction perpendicular to the lines-of-sight. In the blue and red TV data the multiple arc structure is represented sinusoidally by

$$4\pi I_B = 10\,(1 - \cos 2\pi k(x - \nu t))$$

and

$$4\pi I_R = 4\pi I_B/10\,,$$

where $k = 0.1\ \mathrm{km}^{-1}$, $\nu = 7.14$ km/min, and the brightness units are kilo-Rayleighs (kR). The structure is assumed uniform along lines parallel to the lines-of-sight.

Results for the earthlimb radiances calculated on the middle line-of-sight (that is, $x = 0$) on the time interval $0 < t < 16.67$ min are shown on Figure 26. One can see the 2.7 μm emission tracks the temporal structure of the simulated moving auroral arcs. This results from the fact that the response time of the $N(^2D)$ mechanism for 2.7 μm auroral emission, about 0.5 sec at 110 km, is considerably shorter than the period ($\simeq 1.67$ min) of the simulated aurora. The response time for the CO_2 4.3 μm aurora at 110 km is approximately 16 min, considerably longer than the period of the auroral excitation. This explains the temporal behavior of the auroral CO_2 4.3 μm earthlimb radiance as shown on Figure 26. This radiance asymptotically approaches an equilibrium DC level ($\cong 1.8 \times 10^{-7}$ w/cm^2 sr) near $t = 16.67$ min. It also displays a small 1.67 min period ripple in response to the aurora. The amplitude of the CO_2 4.3 μm ripple is about 30 times less than the amplitude of the NO 2.7 μm radiance. Also despite the fact that it is well known that the DC level for vertically viewed auroral CO_2 4.3 μm emission is much larger than for NO auroral 2.7 μm, we see that in viewing on the limb CO_2 4.3 μm self absorption renders the average radiance values about equal for these two emissions.

The steady-state spatial structure at $t = o$ is shown on Figure 27. The positive gradient results from the north sky position of measurements of an arc of 26 October 1978 with respect to the position of the scanning photometer that obtained the data that are used to generate the first frame pair of simulated digitized TV data.

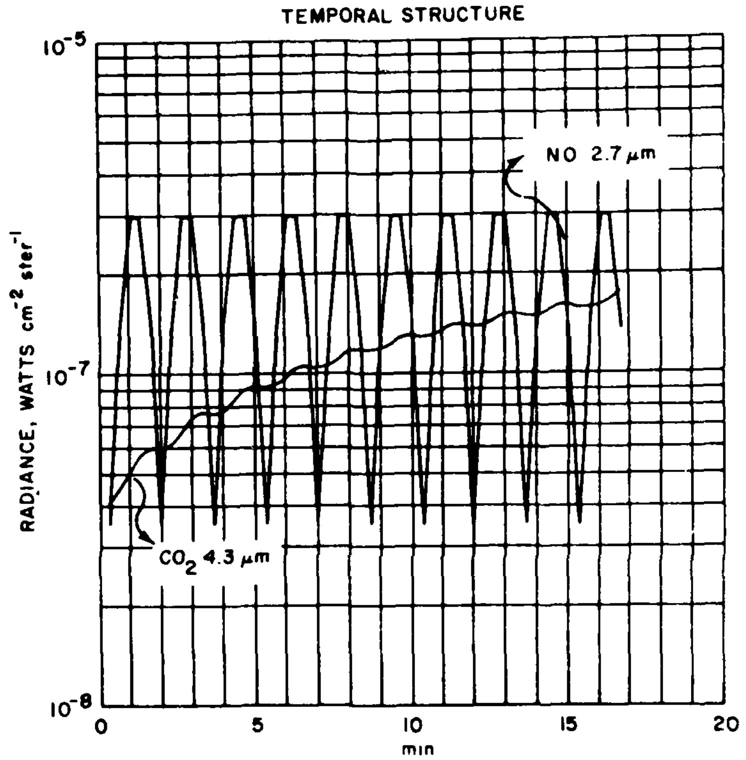

Figure 26. Temporal Dependence on Line-of-Sight Passing Directly Overhead TV Station at 110 km Tangent Altitude on the $0 \leq t \leq 16.63$ min Interval. Projected view direction is approximately 120° southeast of due magnetic north

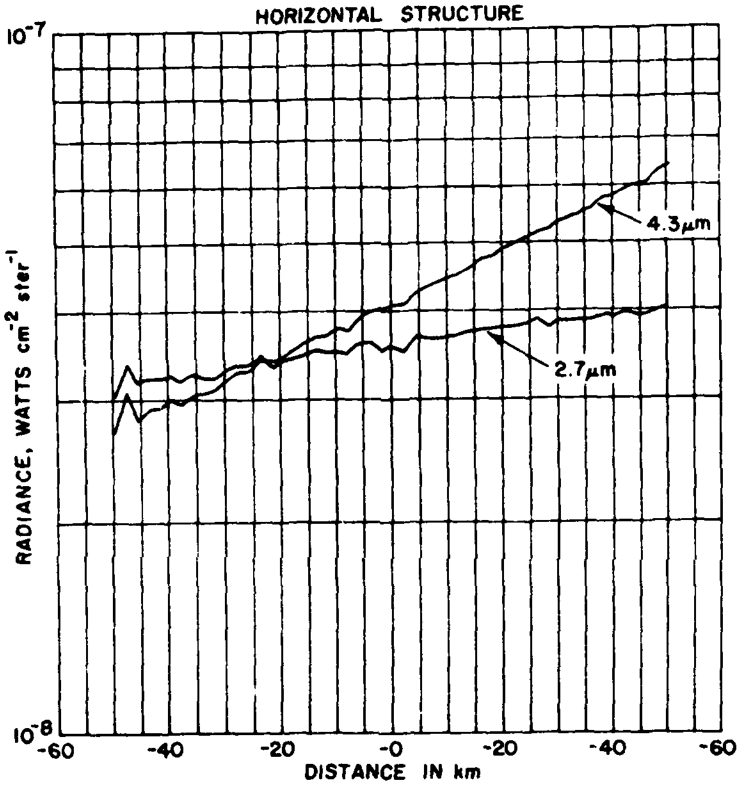

Figure 27. Horizontal Structure in Simulated Steady-State at t = 0, Based on Photometric Data Obtained 26 October 1978 by R. D. Sears[55]

---

[55] Sears, R. D. (1979) Private communication.

References

1. Siebert, M. (1954) Zur theoric der thermischen erregung gezeitenaitiger schwingunger der erdatmosphare. Z. Naturwissenschaften 41:446.
2. Sen, H.K. and White, M.L. (1955) Thermal and gravitational excitation of atmospheric oscillations, J. Geophys. Res. 60:483-485.
3. Chapman, S., and Lindzen, R.S. (1970) Atmospheric Tides, D. Reidel, Hingham, Mass.
4. Forbes, J.M. and Garrett, H.B. (1978) Solar diurnal tide in the thermosphere, J. Atmos. Sci. 35:148-208.
5. Forbes, J.M. and Geller, M.A. (1972) Lunar semidiurnal variation in OI (5577A) nightglow, J. Geophys. Res. 77:2942-2947.
6. Petitdidier, M. and Teitelbaum, H. (1977) Lower thermosphere emissions and tides, Planet Space Sci. 25:711-721.
7. Harris, I. and Mayr, H.G. (1975) Diurnal variations in the thermosphere, J. Geophys. Res. 80:3925-3933.
8. Mayr, H.G. and Harris, I. (1977) Diurnal tide, composition, and winds, J. Geophys. Res. 82:2628-2640.
9. Forbes, J.M. (1978) Tidal variations in thermospheric O, O_2, N_2, Ar, He, and H, J. Geophys. Res. 83:3691-3698.
10. Forbes, J.M. and Marcos, F.A. (1979) Seasonal-latitudinal tidal structures of O, N_2, and total mass density in the thermosphere, J. Geophys. Res. 84:31-35.
11. Hines, C.O. (1960) Internal atmospheric gravity waves at ionospheric heights, Can. J. Phys. 38:1441-1481.
12. Georges, T.M. (1968) HF Doppler studies of traveling ionospheric disturbances, J. Atmos. Terr. Phys. 30:735.
13. Thome, G.D. (1968) Long-period waves generated in the polar ionosphere during the onset of magnetic storms, J. Geophys. Res. 73:6319-6336.
14. Dachs, J. (1968) Die helligkeiten des nachtlichen luftleuchtens wahrend des sommerflechen minimums nach messungen in Sudwestafrika, Beitr. Phys. d. Atmosphare 41:184-215.
15. Armstrong, E.B. (1975) The influence of a gravity wave on the airglow hydroxyl rotational temperature at night, J. Atmos. Terr. Phys. 37:1585-1592.
16. Silverman, S.M. (1962) Unusual fluctuations of 5577Å O I airglow emission intensity on October 28-29, 1961, Nature 195:481-482.
17. Okuda, M. (1962) A study of excitation process in niglet airglow, Sci. Rep. Tohoku Univ. 5th Ser. Geophysics, 14:9-26.
18. Press, F. and Harkrider, D.G. (1962) Propagation of acoustic-gravity waves in the atmosphere, J. Geophys. Res. 67:3889-3908.
19. Pfeffer, R.L. and Zarichny, J. (1963) Acoustic-gravity wave propagation in an atmosphere with two sound channels, Geophys. Pure and Appl. 55:175-199.
20. Harkrider, D.G. and Wells, F.J. (1968) Acoustic-Gravity Waves in the Atmosphere-Symposium Proceedings, T.M. Georges, (ed.) U.S. Government Printing Office, Washington, D.C., pp. 299-314.

21. Friedman, J.P. (1966) Propagation of internal gravity waves in a thermally stratified atmosphere, J. Geophys. Res. 71:1033-1054.

22. Reddy, C.A. (1969) Internal Gravity and Acoustic Waves, A Colloquium, NCAR-TN-43, pp. 229-240.

23. Tuan, T.F. (1976) Research in Gravity Waves and Airglow Phenomena, AFGL-TR-76-0296, AD A040 014.

24. Richmond, A.D. (1978) Gravity wave generation, propagation and dissipation in the thermosphere, J. Geophys. Res. 83:4131-4145.

25. Porter, H.S., Silverman, S.M. and Tuan,T.F. (1974) On the behavior of airglow under the influence of gravity waves, J. Geophys. Res. 79:3827-3833.

26. Peterson, A.W. and Kieffaber, L.M. (1973) Infrared photography of OH airglow structures, Nature 242:321-323.

27. Kieffaber, L.H. and Peterson, A.W. (1978) Correlation studies of four submicron OH airglow bands during spacelab simulation, J. Atmos. Terr. Phys. 40:1339-1345.

28. Peterson, A.W. (1979) Airglow events visible to the naked eye, Applied Optics 18:3390-3393.

29. Chiu, Y.T. and Ching, B.K. (1978) The response of atmosphere and lower ionospheric layer structures to gravity waves, Geophys. Res. Lett. 5:539-542.

30. Hatfield, R., Tuan, T.F. and Silverman, S.M. (1981) On the effects of atmospheric gravity waves on profiles of H, O_3, and OH emission, J. Geophys. Res. 80:2429-2437.

31. Wienstock, J. (1978) Theory of the interaction of gravity waves with $O_2(^1\Sigma)$ airglow, J. Geophys. Res. 83:5175-5185.

32. Hodges, R.R. (1967) Generation of turbulence in the upper atmosphere by internal gravity waves, J. Geophys. Res. 72:3455-3458.

33. Tuan, T.F., Hedinger, R., Silverman, S.M. and Okuda, M. (1979) On gravity wave induced Brunt-Vaisala oscillations, J. Geophys. Res. 84:393-398.

34. Philbrick, C.R., Noonan, J.P., Fletcher, E.T., Jr., Hanrahan, T., Salah, J.E., Blood, D.W., Olsen, R.O. and Kennedy, B.W. (1978) Atmospheric Properties From Measurements at Kwajalein Atoll on 5 April 1978, AFGL-TR-0195, AD A061 083.

35. Hines, C.O. (1974) The Upper Atmosphere in Motion, American Geophysical Union Monograph 18.

36. Davis, M.J. and Da Rosa, A.V. (1969) Traveling ionospheric disturbances originating in the auroral oval during polar substorms, J. Geophys. Res. 74:5721-5735.

37. Newton, G.P., Kasprzak, W.T., Curtis, S.A. and Pelz, D.J. (1975) Local time variation of equatorial thermospheric composition determined by the San Marco 3 Nace, J. Geophys. Res. 80:2289-2299.

38. Sharp, L.R., Hickman, D.R., Rice, C.J. and Straus, J.M. (1978) The altitude dependence of the local time variation of thermospheric density, Geophys. Res. Lett. 5:261-263.

39. Philbrick, C.R., Murphy, E.A., Zimmerman, S.P., Fletcher, E.J., Jr., and Olsen, R.O. (1980) Mesospheric density variability, Space Research XX:79-82.

40. Howlett, L.C., Baker, K.D., Megill, L.R., Shaw, A.W., and Pendleton, W.R. (1980) Measurement of a structured profile of atomic oxygen in the mesosphere and lower thermosphere, J. Geophys. Res. 85:1291-1298.

41. Keneshea, T.J., Zimmerman, S.P. and Philbrick, C.R. (1979) A dynamic model of the mesosphere and lower thermosphere, Planet. Space Sci. 27:385-401.

42. McIssac, J.P. (1980) Private communication.

43. Reber, C.A., Hedin, A.E., Pelz, D.T., Potter, W.E. and Brace, L.H. (1975) Phase and amplitude relationships of wave structure observed in the lower thermosphere, J. Geophys. Res. 80:4576-4580.

44. Potter, W.E., Kayser, D.C. and Mauersberger, K. (1976) Direct measurements of neutral wave characteristics in the thermosphere, J. Geophys. Res. 81:5002-5012.

45. Trinks, H., Mayr, H.G. and Philbrick, C.R. (1978a) Momentum source signatures in thermospheric neutral composition, J. Geophys. Res. 83:1641-1646.

46. Trinks, H., Offerman, D., von Zahn, U. and Steinhauer, C. (1978b) Neutral composition measurements between 90 and 220 km altitude by rocket-borne mass spectrometer, J. Geophys. Res. 83:2169-2176.

47. Philbrick, C.R., Faire, A.E., and Fryklund, D.H. (1978a) Measurements of Atmospheric Density at Kwajalein Atoll, 18 May 1977, AFGL-TR-0058, AD A054 784.

48. Philbrick, C.R. (1976) Recent satellite measurement of upper atmospheric composition, Space Research XVI:289-295.

49. Philbrick, C.R. (1980) Private communication.

50. Titus, J. and Anapol, M. (1979) Private communication.

51. Huffman, R.E., LeBlanc, F.J., Larrabee, J.C. and Paulsen, D.E. (1979) Satellite Atmospheric Radiance Measurements in the Vacuum Ultraviolet, AFGL-TR-79-0151, AD A078 628.

52. N.B.S. (1962) Auroral arcs in mid-latitudes, National Bureau of Standards Technical News Bulletin 46:42-46.

53. Rees, M.H. and Luckey, D. (1974) Auroral electron energy derived from ratio of spectroscopic emissions, J. Geophys. Res. 79:5181-5186.

54. Kumer, J.B. (1977) Further Evaluation of ICECAP Auroral 4.3 μm Zenith Radiance, Haes Report No. 57 DNA 4260F.

55. Sears, R.D. (1979) Private communication.